

# A TRIDENT SCHOLAR PROJECT REPORT

NO. 438

---

**An Examination of a Pumping Rotor Blade Design for Brownout Mitigation**

by

Midshipman 1/C Daniel R. Kuerbitz, USN

---



UNITED STATES NAVAL ACADEMY  
ANNAPOLIS, MARYLAND

This document has been approved for public  
release and sale; its distribution is limited.

USNA-1531-2

**AN EXAMINATION OF A PUMPING ROTOR BLADE DESIGN  
FOR BROWNOUT MITIGATION**

by

Midshipman 1/C Daniel R. Kuerbitz  
United States Naval Academy  
Annapolis, Maryland

---

(signature)

Certification of Adviser(s) Approval

Assistant Professor Joseph I. Milluzzo  
Aerospace Engineering Department

---

(signature)

---

(date)

Associate Professor David S. Miklosovic  
Aerospace Engineering Department

---

(signature)

---

(date)

Acceptance for the Trident Scholar Committee

Professor Maria J. Schroeder  
Associate Director of Midshipman Research

---

(signature)

---

(date)

REPORT DOCUMENTATION PAGE				Form Approved OMB No. 0704-0188	
Public reporting burden for this collection of information is estimated to average 1 hour per response, including the time for reviewing instructions, searching existing data sources, gathering and maintaining the data needed, and completing and reviewing this collection of information. Send comments regarding this burden estimate or any other aspect of this collection of information, including suggestions for reducing this burden to Department of Defense, Washington Headquarters Services, Directorate for Information Operations and Reports (0704-0188), 1215 Jefferson Davis Highway, Suite 1204, Arlington, VA 22202-4302. Respondents should be aware that notwithstanding any other provision of law, no person shall be subject to any penalty for failing to comply with a collection of information if it does not display a currently valid OMB control number. <b>PLEASE DO NOT RETURN YOUR FORM TO THE ABOVE ADDRESS.</b>					
1. REPORT DATE (DD-MM-YYYY) 05-18-2015		2. REPORT TYPE		3. DATES COVERED (From - To)	
4. TITLE AND SUBTITLE An Examination of a Pumping Rotor Blade Design for Brownout Mitigation				5a. CONTRACT NUMBER	
				5b. GRANT NUMBER	
				5c. PROGRAM ELEMENT NUMBER	
6. AUTHOR(S) Kuerbitz, Daniel Richard				5d. PROJECT NUMBER	
				5e. TASK NUMBER	
				5f. WORK UNIT NUMBER	
7. PERFORMING ORGANIZATION NAME(S) AND ADDRESS(ES)				8. PERFORMING ORGANIZATION REPORT NUMBER	
9. SPONSORING / MONITORING AGENCY NAME(S) AND ADDRESS(ES) U.S. Naval Academy Annapolis, MD 21402				10. SPONSOR/MONITOR'S ACRONYM(S)	
				11. SPONSOR/MONITOR'S REPORT NUMBER(S) Trident Scholar Report no. 438 (2015)	
12. DISTRIBUTION / AVAILABILITY STATEMENT  This document has been approved for public release; its distribution is UNLIMITED.					
13. SUPPLEMENTARY NOTES					
14. ABSTRACT Brownout is a significant concern for Naval rotorcraft operations. It occurs when a rotorcraft operates over an unprepared surface and becomes engulfed in a cloud of sediment. High resolution flow visualization (FV) and particle image velocimetry (PIV) measurements were taken to examine the development and evolution of rotor tip vortices. The current work focuses on diffusing tip vortices through the use of pumping rotor blades, as the tip vortices are the primary means of sediment uplift. A baseline non-pumping and four pumping blade designs were tested. All the pumping blade designs used a centrifugal pumping design, but the internal flow exited the blade tips at orientations of 0°, 30°, 45°, and 60° above the horizontal axis. All blade designs were tested in a hovering state in ground effect at a blade loading coefficient of 0.08. Additional measurements were performed on the baseline and 0° pumping blades at a lower blade loading coefficient of 0.053, which was considered the functional equivalent of testing a higher mass flow through the pumping slots. The pumping blades experienced a power penalty in comparison to the baseline, which was a result of profile losses due to the exit slots at the tip. When operating at the higher thrust condition, the pumping blades were found to merely prolong the initial formation of the tip vortices, rather than completely diffusing them. However, the 0° pumping blade was found to generate significantly diffused tip vortices at the lower thrust condition, which greatly reduced upwash velocities near the ground.					
15. SUBJECT TERMS brownout, vortex diffusion, pumping blade					
16. SECURITY CLASSIFICATION OF:			17. LIMITATION OF ABSTRACT	18. NUMBER OF PAGES  77	19a. NAME OF RESPONSIBLE PERSON
a. REPORT	b. ABSTRACT	c. THIS PAGE			19b. TELEPHONE NUMBER (include area code)

## ABSTRACT

Brownout is a significant concern for Naval rotorcraft operations. It occurs when a rotorcraft operates over an unprepared surface and becomes engulfed in a cloud of sediment. High resolution flow visualization (FV) and particle image velocimetry (PIV) measurements were taken to examine the development and evolution of rotor tip vortices. The current work focuses on diffusing tip vortices through the use of pumping rotor blades, as the tip vortices are the primary means of sediment uplift. A baseline non-pumping and four pumping blade designs were tested. All the pumping blade designs used a centrifugal pumping design, but the internal flow exited the blade tips at orientations of  $0^\circ$ ,  $30^\circ$ ,  $45^\circ$ , and  $60^\circ$  above the horizontal axis. Detailed flow measurements were performed in regions of interest near the rotor and near the ground plane. All blade designs were tested in a hovering state in ground effect at a blade loading coefficient,  $C_T/\sigma$ , of 0.08. Additional measurements were performed on the baseline and  $0^\circ$  pumping blades at a lower blade loading coefficient of 0.053, which was considered the functional equivalent of testing a higher mass flow through the pumping slots. Performance measurements were also taken. The pumping blades experienced a power penalty in comparison to the baseline, which was a result of profile losses due to the exit slots at the tip. Additionally, the  $30^\circ$ ,  $45^\circ$ , and  $60^\circ$  pumping blades suffered degraded performance in comparison to the  $0^\circ$  pumping blade due to a negative thrust effect that resulted from mass flow through the pumping slots. When operating at the higher thrust condition, the pumping blades were found to merely prolong the initial formation of the tip vortices, rather than completely diffusing them. However, the  $0^\circ$  pumping blade was found to generate significantly diffused tip

vortices at the lower thrust condition, which greatly reduced upwash velocities near the ground.

Keywords: Brownout, Vortex Diffusion, Pumping Blade

## ACKNOWLEDGMENTS

First and foremost, I would like to thank my advisers, Assistant Professor Joseph Milluzzo and Associate Professor David Miklosovic. Their expertise, advice, and dedication were instrumental to the success of the project.

I would also like to thank Dr. J. Gordon Leishman of Embry-Riddle Aeronautical University and the University of Maryland's Alfred Gessow Rotorcraft Center, who provided the facilities needed to collect the data for this experiment. Additionally, I would like to thank Dr. Dancilia of the University of Texas at Austin, who provided the pumping blades.

The Rickover Computer Support Branch went to great lengths to meet the considerable technical demands posed by my project. Special thanks goes to John Wilcox, who helped build or manage several machines used to process the massive amounts of data gathered in this project.

I would like to thank the Office of Naval Research, which helped fund this project, as well as LtCol (ret) Scott Davids, who fully supported this project as the leader of the newly established USNA Rotorcraft Engineering program.

Finally, I would like to thank Professor Maria Schroeder and the Trident Committee for the opportunity to pursue this research project and the guidance to make it successful.

## CONTENTS

<i>Contents</i> . . . . .	4
<i>List of Tables</i> . . . . .	6
<i>List of Figures</i> . . . . .	7
<i>1. Introduction</i> . . . . .	13
1.1 Fluid Mechanics of Brownout . . . . .	15
1.2 In-Ground-Effect Fluid Mechanics . . . . .	16
1.3 Dual Phase Fluid Mechanics . . . . .	19
1.4 Diffusion of Tip Vortices . . . . .	20
1.5 Objectives . . . . .	24
<i>2. Description of Experiment</i> . . . . .	26
2.1 Blade Tips . . . . .	27
2.2 Theory . . . . .	29
2.3 Performance Measurements . . . . .	31
2.4 Flow Field Measurements . . . . .	32
2.4.1 PIV Imaging . . . . .	33

2.5 Data Analysis . . . . .	35
3. <i>Results</i> . . . . .	37
3.1 Performance Results . . . . .	37
3.2 Flow Visualization . . . . .	39
3.3 Instantaneous Flow Field Measurements . . . . .	42
4. <i>Conclusions</i> . . . . .	69
4.1 Recommendations for Future Work . . . . .	71
<i>References</i> . . . . .	73



## LIST OF TABLES

2.1	Summary of rotor characteristics and test conditions . . . . .	27
3.1	Force generated by mass flow and normalized induced power factor for the four pumping blade designs . . . . .	39

## LIST OF FIGURES

1.1	A helicopter landing and encountering brownout conditions. U.S. Air Force photo by Staff Sgt. Christopher Boitz. . . . .	14
1.2	Scaled comparison of a rotor hovering (a) out of ground effect and (b) in ground effect [1]. Used with permission. . . . .	17
1.3	A rotor in reference position $\psi_b$ , shedding a wake of wake age $\zeta$ [2] . . .	18
1.4	Mechanisms of sediment entrainment (Sydney et al. [3]) . . . . .	20
1.5	The four blade types tested by Milluzzo et al. [4], with blade tips on the right [4] . . . . .	21
1.6	Detail of the slotted blade tip design [5,6]. Used with permission. . . . .	22
1.7	The centrifugal pumping slotted blade design . . . . .	24
2.1	Basic test setup [4] . . . . .	28
2.2	Exit slot orientation . . . . .	28
2.3	The test setup for flow field measurements [2] . . . . .	33
2.4	The two regions of interest (ROIs) examined in the experiment . . . . .	35
3.1	Plot of the measured power polar for each rotor. . . . .	38

- 3.2 Representative flow visualization with the reference blade at a blade azimuth angle  $\psi_b$  of  $30^\circ$  and the rotor operating at a  $C_T/\sigma = 0.080$ , for the: (a) Baseline non-pumping blade (b)  $0^\circ$  exit slot orientation, (c)  $30^\circ$  exit slot orientation, (d)  $45^\circ$  exit slot orientation, and (e) the  $60^\circ$  exit slot orientation. . . . . 40
- 3.3 Representative flow visualization of the baseline blade for each operating condition at  $\psi_b = 30^\circ$ : (a)  $C_T/\sigma = 0.053$ ; (b)  $C_T/\sigma = 0.080$ . . . . . 43
- 3.4 Representative flow visualization of the  $0^\circ$  pumping blade for each operating condition at  $\psi_b = 30^\circ$ : (a)  $C_T/\sigma = 0.053$ ; (b)  $C_T/\sigma = 0.080$ . . . . . 43
- 3.5 Contours of instantaneous vorticity in ROI 1, with the reference blade at a blade azimuth angle  $\psi_b$  of  $30^\circ$  and the rotor operating at a  $C_T/\sigma = 0.080$ , for the: (a) Baseline non-pumping blade; (b)  $0^\circ$  exit slot orientation; (c)  $30^\circ$  exit slot orientation; (d)  $45^\circ$  exit slot orientation; and (e) the  $60^\circ$  exit slot orientation. . . . . 45
- 3.6 Contours of non-dimensionalized total velocity in ROI 1, with the reference blade at a blade azimuth angle  $\psi_b$  of  $30^\circ$  and the rotor operating at a  $C_T/\sigma = 0.080$ , for the: (a) Baseline non-pumping blade; (b)  $0^\circ$  exit slot orientation; (c)  $30^\circ$  exit slot orientation; (d)  $45^\circ$  exit slot orientation; and (e) the  $60^\circ$  exit slot orientation. . . . . 46
- 3.7 Contours of instantaneous vorticity in ROI 1, for the rotor with the baseline blades at  $\psi_b = 30^\circ$  for each operating condition: (a)  $C_T/\sigma = 0.053$ ; (b)  $C_T/\sigma = 0.080$ . . . . . 47

3.8	Contours of non-dimensionalized total velocity in ROI 1, for the rotor with the baseline blades at $\psi_b = 30^\circ$ for each operating condition: (a) $C_T/\sigma = 0.053$ ; (b) $C_T/\sigma = 0.080$ . . . . .	48
3.9	Contours of non-dimensionalized total velocity in ROI 1, for the rotor with the $0^\circ$ pumping blades at $\psi_b = 30^\circ$ for each operating condition: (a) $C_T/\sigma = 0.053$ ; (b) $C_T/\sigma = 0.080$ . . . . .	49
3.10	Contours of non-dimensionalized total velocity in ROI 1, for the rotor with the $0^\circ$ pumping blades at $\psi_b = 30^\circ$ for each operating condition: (a) $C_T/\sigma = 0.053$ ; (b) $C_T/\sigma = 0.080$ . . . . .	50
3.11	Representative swirl velocity profile plotted across a tip vortex . . . . .	52
3.12	Swirl velocity profiles at early wake ages ( $\zeta \leq 150^\circ$ ) operating at $C_T/\sigma = 0.08$ for (a) the baseline blade and (b) the $0^\circ$ pumping blade. . . . .	53
3.13	Swirl velocity profiles at later wake ages ( $\zeta \geq 180^\circ$ ) operating at $C_T/\sigma = 0.08$ for (a) the baseline blade and (b) the $0^\circ$ pumping blade. . . . .	53
3.14	Swirl velocity profiles at early wake ages ( $\zeta \leq 150^\circ$ ) operating at $C_T/\sigma = 0.053$ for (a) the baseline blade and (b) the $0^\circ$ pumping blade. . . . .	54
3.15	Swirl velocity profiles at later wake ages ( $\zeta \geq 180^\circ$ ) operating at $C_T/\sigma = 0.053$ for (a) the baseline blade and (b) the $0^\circ$ pumping blade. . . . .	55
3.16	Contours of instantaneous vorticity near the ground (ROI 2), with the reference blade at a blade azimuth angle ( $\psi_b$ ) of $30^\circ$ and the rotor operating at a $C_T/\sigma = 0.080$ , for the:(a) Baseline non-pumping blade; (b) $0^\circ$ exit slot orientations; (c) $30^\circ$ exit slot orientations; (d) $45^\circ$ exit slot orientations; and (e) the $60^\circ$ exit slot orientations. . . . .	57

- 3.17 Contours of non-dimensionalized wall-normal velocity near the ground (ROI 2), with the reference blade at a blade azimuth angle ( $\psi_b$ ) of  $30^\circ$  and the rotor operating at a  $C_T/\sigma = 0.080$ , for the: (a) Baseline non-pumping blade; (b)  $0^\circ$  exit slot orientations; (c)  $30^\circ$  exit slot orientations; (d)  $45^\circ$  exit slot orientations; and (e) the  $60^\circ$  exit slot orientations. . . . . 58
- 3.18 Contours of instantaneous vorticity near the ground (ROI 2), for the rotor with the baseline blades at  $\psi_b = 30^\circ$  for each operating condition: (a)  $C_T/\sigma = 0.053$ ; (b)  $C_T/\sigma = 0.080$ . . . . . 59
- 3.19 Contours of non-dimensionalized wall-normal velocity near the ground (ROI 2), for the rotor with the baseline blades at  $\psi_b = 30^\circ$  for each operating condition: (a)  $C_T/\sigma = 0.053$ ; (b)  $C_T/\sigma = 0.080$ . . . . . 60
- 3.20 Contours of instantaneous vorticity near the ground (ROI 2), for the rotor with the  $0^\circ$  pumping blades at  $\psi_b = 30^\circ$  for each operating condition: (a)  $C_T/\sigma = 0.053$ ; (b)  $C_T/\sigma = 0.080$ . . . . . 61
- 3.21 Contours of non-dimensionalized wall-normal velocity near the ground (ROI 2), for the rotor with the  $0^\circ$  pumping blades at  $\psi_b = 30^\circ$  for each operating condition: (a)  $C_T/\sigma = 0.053$ ; (b)  $C_T/\sigma = 0.080$ . . . . . 62
- 3.22 Representative wall velocity profiles plotting wall-normal velocity in the flow field. Cut A intersects a tip vortex, while there is no tip vortex present in Cut B. . . . . 63

- 3.23 Velocity profiles for the baseline, non-pumping blade at  $C_T/\sigma = 0.08$ :  
 (a) Wall-parallel velocities with no tip vortex present, (b) Wall-parallel velocities with a tip vortex present, (c) Wall-normal velocities with no tip vortex present, and (d) Wall-normal velocities with a tip vortex present. . . . . 65
- 3.24 Velocity profiles for the  $0^\circ$  pumping blade at  $C_T/\sigma = 0.08$ : (a) Wall-parallel velocities with no tip vortex present, (b) Wall-parallel velocities with a tip vortex present, (c) Wall-normal velocities with no tip vortex present, and (d) Wall-normal velocities with a tip vortex present. . . . . 66
- 3.25 Velocity profiles for the baseline, non-pumping blade at  $C_T/\sigma = 0.053$ :  
 (a) Wall-parallel velocities with no tip vortex present, (b) Wall-parallel velocities with a tip vortex present, (c) Wall-normal velocities with no tip vortex present, and (d) Wall-normal velocities with a tip vortex present. . . . . 67
- 3.26 Velocity profiles for the  $0^\circ$  pumping blade at  $C_T/\sigma = 0.053$ : (a) Wall-parallel velocities with no tip vortex present, (b) Wall-parallel velocities with a tip vortex present, (c) Wall-normal velocities with no tip vortex present, and (d) Wall-normal velocities with a tip vortex present. . . . . 68

## LIST OF SYMBOLS

$A$	Rotor disk area, $\pi R^2$ , $\text{m}^2$
$c$	blade chord, m
$C_T$	Rotor thrust coefficient, $= T / \rho \pi \Omega^2 R^4$
$C_P$	Rotor power coefficient, $= P / \rho \pi \Omega^3 R^5$
$C_T / \sigma$	Blade loading coefficient
$C_P / \sigma$	Power loading coefficient
$N_b$	Number of blades
$r$	Radial distance, m
$R$	Radius of blade, m
$T$	Rotor thrust, N
$u, v$	Velocities in the $r$ and $z$ directions, $\text{ms}^{-1}$
$V_{\text{tip}}$	Rotor tip speed, $\Omega R$ , $\text{ms}^{-1}$
$z$	Distance from rotor plane, m
$\zeta$	Wake age, deg
$\theta_e$	Slot exit orientation angle, deg
$\rho$	Flow density
$\sigma$	Rotor solidity $= N_b c / \pi R$
$\psi_b$	Blade azimuth angle, deg
$\Omega$	Rotational speed of the rotor, $\text{s}^{-1}$

## 1. INTRODUCTION

When a vehicle travels through the air, it leaves a wake, or a trail of disturbed air. The wake of a fixed wing aircraft convects behind the vehicle, so the wake has only a small direct effect on the aircraft. In contrast, the wake shed by a rotorcraft remains near the vehicle and can greatly affect the vehicle's operation. Rotor blades generate highly three-dimensional vortical wakes. These wakes, and specifically the trailed tip vortices, contribute to several undesirable rotor behaviors, including but not limited to unsteady airloads, noise caused by blade-vortex interactions (BVI), vibrations, and brownout. In particular, brownout poses significant safety risks to both civilian and military operations. It is especially relevant to current military operations, as brownout most readily occurs on unprepared landing zones covered by dry, loose sediment.

Brownout occurs when the rotor wake interacts with the sediment bed to uplift and suspend loose sediment in the air in close proximity to the vehicle, creating a dust cloud. Figure 1.1 depicts a helicopter operating in brownout conditions. Brownout poses significant short- and long-term risks to rotorcraft operation. In the short term, the brownout cloud obscures the pilot's vision, resulting in the loss of necessary visual cues. The absence of these cues greatly increases the risk of accidents. The brownout cloud can also createvection illusions, giving the pilot the impression of motion when the vehicle is stationary, or vehicle drift, when the pilot is unaware of the aircraft's motion [7, 8]. Vection





*Fig. 1.1: A helicopter landing and encountering brownout conditions. U.S. Air Force photo by Staff Sgt. Christopher Boitz.*

illusions and vehicle drift can result in collisions or damaged landing gear. In fact, it is reported that brownout is responsible for up to 60% of military operational mishaps in which human factors play a role [9, 10]. Brownout also poses significant risks to civilian rotorcraft operations, such as search and rescue missions over unprepared surfaces. Additionally, brownout poses serious hazards to ground personnel working in close proximity to the rotorcraft, where the high winds and dust cloud can damage equipment, reduce visibility for ground workers, and lead to injury. Long-term effects of brownout are no less undesirable, as they significantly reduce operational efficiency. Uplifted sediment can damage engine components and sensitive equipment. In particular, brownout significantly reduces the service life of rotor blades. Consequently, The adverse effects of brownout on rotorcraft operations make it desirable to gain a better aerodynamic understanding of the factors affecting brownout, namely the interaction of the rotor wake and the ground.

## 1.1 *Fluid Mechanics of Brownout*

Brownout is caused by the interaction of the rotor wake with the ground. The wake generated by a hovering rotor is dominated by tip vortices, which form when the higher pressure air on the underside of the blade convects around the tip to the lower pressure air above the blade, resulting in a circulatory flow. Each rotor blade trails a single concentrated tip vortex, which forms a continuous vortex filament that follows a helicoidal trajectory as it convects in the wake. These tip vortices convect along the slipstream boundary, which separates regions of turbulent, high energy flow inside the rotor wake and low energy, quiescent flow outside the wake.

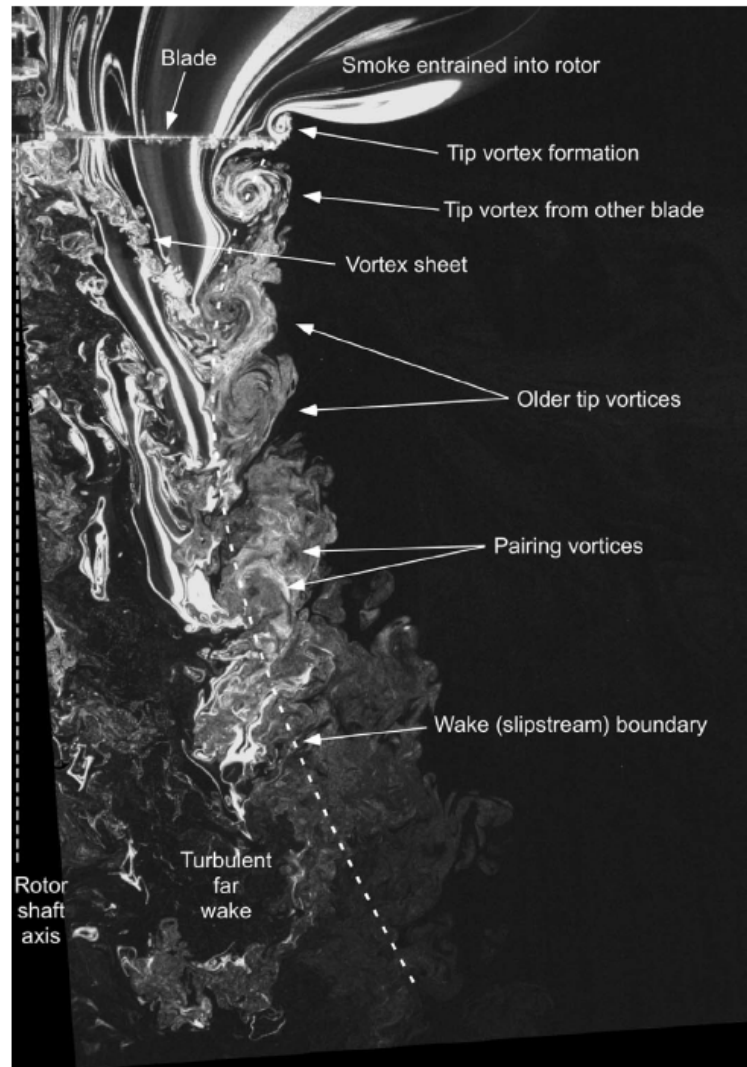
The structure of the rotor wake is significantly affected by the rotor's proximity to the ground. A rotor is considered to be operating in ground effect (IGE) when it operates less than one rotor radius from the ground, and out of ground effect (OGE) at altitudes greater than one rotor diameter. Fig. 1.2a shows smoke flow visualization of the wake generated by a two bladed rotor system hovering OGE. The image is a visualization of a planar cut of the rotor wake intersecting the axis of rotation such that a trailed vortex appears every time a blade passes through the plane. The tip vortices exert centrifugal and Coriolis forces on the seed particles in the flow, so that vortices are characterized by the presence of seed voids. Each blade trailed a single helicoidal tip vortex which intersected the plane at intervals of  $360/N_b$ , where  $N_b$  is the number of blades on the rotor (e.g., intersections at blade position  $\psi_b = 30^\circ$  would show vortices of wake ages  $\zeta = 30^\circ$ ,  $210^\circ$ ,  $390^\circ$ , etc.). The intersections are measurements of wake age,  $\zeta$ , which is defined as the elapsed time since a flow structure was convected by the rotor blade. Wake age

is measured in terms of rotor position  $\psi_b$ , as shown in Fig. 1.3 (e.g., a vortex one rotor revolution old would have a wake age of  $360^\circ$ ).

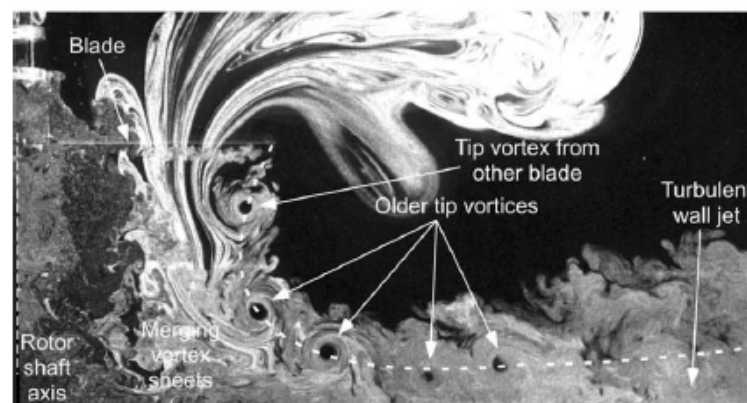
Fig. 1.2a shows that for a rotor operating OGE, the wake convects axially below the rotor, first contracting and then expanding. Tip vortices diffuse after two or three rotor revolutions (i.e., four to six distinct vortices are shown for the two bladed system in Fig. 1.2a). Far downstream, the diffused tip vortices contribute to the turbulent wake, creating a turbulent jet-like flow. In contrast, the wake of a rotor operating IGE interacts with the ground, changing its structure. The ground is a streamline to the wake of a rotor operating IGE, so the wake must rapidly turn from a primarily axial flow to a primarily radial flow, as demonstrated in Fig. 1.2b. Ramasamy et al. [11] showed that as the wake and the tip vortex filaments expand radially, the filaments stretch. Conservation of mass requires that the filament core contracts, and the swirl velocity and vorticity of the vortex increases in order to conserve momentum. This process is known as reintensification [11]. Fig. 1.2b shows that reintensification causes the vortices of a rotor operating IGE to persist to older wake ages than those of a rotor operating OGE.

## 1.2 *In-Ground-Effect Fluid Mechanics*

Lee et al. [1] were among the first to experimentally examine the fluid mechanics of the interaction between a small-scale rotor and a ground plane. They performed both particle image velocimetry (PIV) experiments, in which a strobed laser sheet illuminated tracer (or seed) particles in the flow, and qualitative analysis via flow visualization, which examined the rotor wake at a variety of wake ages and rotor altitudes. The experiment



(a) Out of ground effect



(b) In ground effect

Fig. 1.2: Scaled comparison of a rotor hovering (a) out of ground effect and (b) in ground effect

[1]. Used with permission.

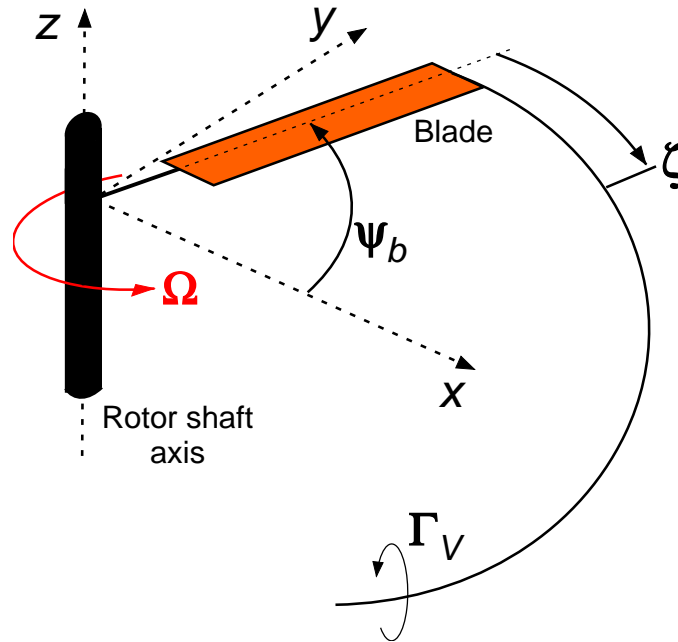


Fig. 1.3: A rotor in reference position  $\psi_b$ , shedding a wake of wake age  $\zeta$  [2]

confirmed that the OGE rotor produced tip vortices that diffused within three rotor revolutions, yielding a jet-like flow in the far wake, while the IGE rotor produced vortices which stretched along their lengths, reintensified their vorticity, and increased swirl velocities. The reintensified tip vortices persisted to older wake ages and caused the flow at the ground to become a superposition of coherent tip vortices and a developing wall-jet type flow. The interaction of the rotor wake with the ground plane created a turbulent boundary layer along the ground plane, so that the structure and strength of the wake at the ground directly affected the shear stress exerted on the ground plane (and on a sediment bed). In summary, Lee et al. showed that in comparison to OGE operations, the wake of a rotor operating in ground effect retained and reintensified its vorticity, causing the tip vortices to persist to older wake ages. The persistent tip vortices greatly affected the development, structure, velocities, and turbulence observed in the wake along the ground.

### 1.3 *Dual Phase Fluid Mechanics*

Johnson et al. [12] and Sydney et al. [3] investigated the dual-phase fluid mechanics of brownout, with air as the carrier phase and sediment as the dispersed phase. They investigated the interaction between the rotor wake and the sediment to determine the mechanisms by which sediment is entrained into the airflow. Six mechanisms were identified and are detailed in Fig. 1.4. All six were direct results of the tip vortices: creep, saltation and bombardment, vortex induced trapping, secondary suspension, vortex induced bombardment, and unsteady pressure effects. Creep is the mobilization of sediment particles along the ground. Some sediment particles are light enough to be uplifted, but ultimately fall back to the sediment bed. Johnson et al. observed that when the uplifted particles impacted the sediment bed, they uplifted more sediment particles. This process, known as saltation bombardment, can significantly increase the number of particles introduced into the flow. Vortex induced trapping refers to the uplift of particles entrained in the flow by the upward swirl velocities of a vortex. If the uplifted particles are suspended by a second, younger vortex, then secondary suspension occurs. Conversely, vortex induced bombardment occurs when downward swirl velocities drive suspended sediment particles into the ground, ejecting more sediment particles. Finally, tip vortices convecting along the ground can create unsteady pressure effects. This final mechanism was hypothesized, but not directly observed. Since all the mechanisms of sediment entrainment are dependent on the intensity of the tip vortices in the wake, it is expected that a reduction in tip vortex intensity may reduce the amount of sediment uplifted.

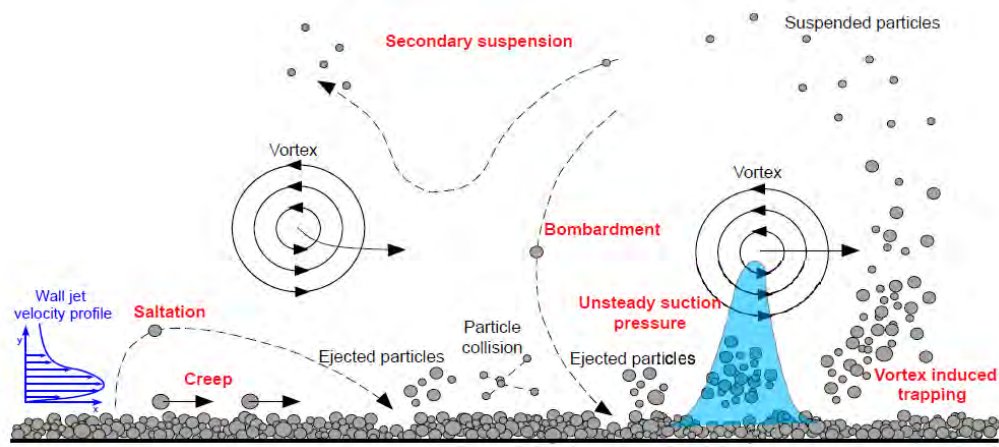
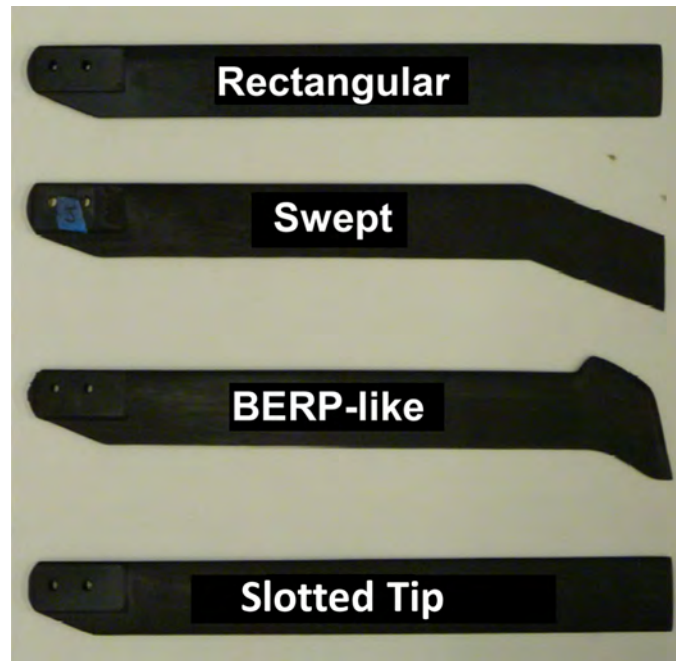


Fig. 1.4: Mechanisms of sediment entrainment (Sydney et al. [3])

## 1.4 Diffusion of Tip Vortices

Johnson et al. [12] and Sydney et al. [3] demonstrated that tip vortices were the primary cause of sediment mobilization and entrainment. It is therefore expected that one method to reduce the effects of brownout is to diffuse the concentrated tip vortices in the rotor wake before they reach the ground. There are two methods used to diffuse tip vortices: active and passive. Active methods modify the shape of the blade and/or control the airflow using actuators [17]. Passive methods modify the blade tip to alter the rollup and formation of tip vortices. Milluzzo et al. [4] studied passive vortex diffusion methods using PIV. Four tip shapes were tested: a rectangular tip used as a baseline, a simple swept tip, a BERP-like tip [13] (British Experimental Rotor Program, a rotor tip design optimized for high speed operations), and a slotted tip [5, 6, 14]. Fig. 1.5 shows the four blade designs. The slotted blade is detailed in Fig. 1.6. This blade was designed with slots which connect holes on the leading edge of the blade to holes on the side of the blade at the tip. The high dynamic pressure at the blade tip forced air in at the leading



*Fig. 1.5:* The four blade types tested by Milluzzo et al. [4], with blade tips on the right [4]

edge and ejected turbulence from the tip, into the forming vortex core. This turbulence modified the core structure and caused rapid diffusion of vorticity [14].

Milluzzo et al. [4] expanded on previous work in several ways. The experiment used a larger rotor (the rotor radius was 16 inches, while previous experiments used a 3.35 inch radius), which allowed study of vortical effects of the rotor wake at higher Reynolds numbers. The experiment investigated both the development of the rotor wake in ground effect and the effect of different blade tip designs on the wake. The rectangular tip was used as a baseline. It produced strong, concentrated tip vortices that ultimately reintensified near the ground and induced strong velocities in the axial and radial directions. The simple swept tip produced tip vortices which behaved similarly to those convected by the baseline blade. The BERP-like blade tip modified the rollup of tip vortices such that they were initially more diffused, but interaction with the ground plane and stretching of



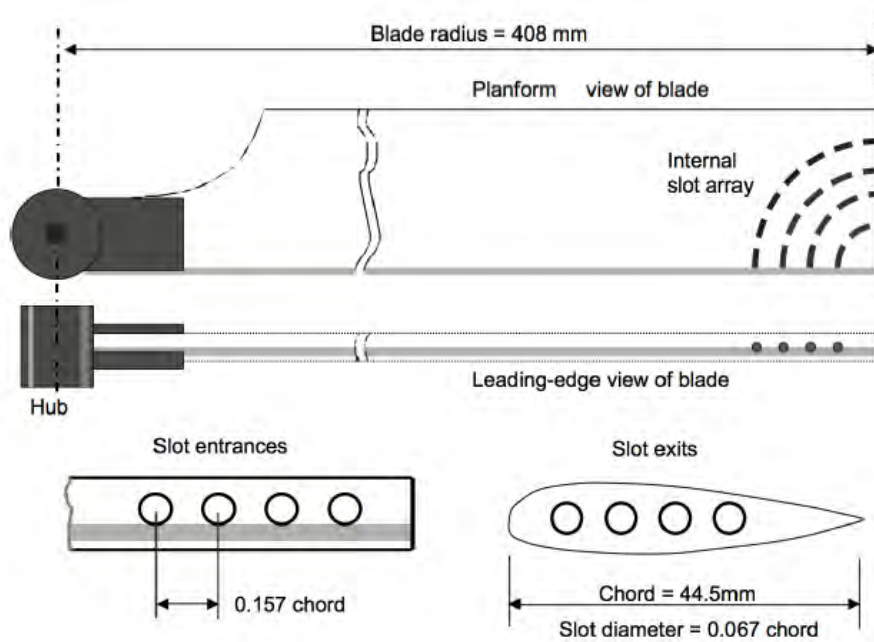


Fig. 1.6: Detail of the slotted blade tip design [5,6]. Used with permission.

the vortex filaments ultimately caused the tip vortices to reintensify, such that at older wake ages there was little difference between the vortices convected by the BERP-like tip, the simple swept tip, and the rectangular tip. Because the tip vortex characteristics of these blade designs were similar, it is expected that they would all have similar brownout characteristics. In contrast, the slotted blade tip design produced significantly diffused vortices at all wake ages. The vortices were sufficiently diffused so that they did not reintensify in ground effect, resulting in lower peak velocities in the developing flow near the ground plane. It is expected that the slotted tip would produce a less intense brownout signature. However, while the slotted tip design exhibited desirable vortex diffusion characteristics, it also incurred a 2% power penalty in comparison to the baseline blade. In other words, for a given thrust output, the slotted blade tip required 2% greater power than the rectangular tip. This power penalty resulted from the increased profile drag due

to the tip slots. In rotorcraft operations, the power penalty would significantly hamper rotorcraft performance characteristics such as payload and speed. Therefore, Milluzzo et al. concluded that while only the slotted tip effectively diffused tip vortices, the associated power penalty reduced the design's desirability as a solution to the problem of brownout.

The slotted tip design used by Milluzzo et al. [4] diffused vortices by ejecting turbulent air out of exit slots at the tip. To achieve this, the blade had intake slots on the leading edge, which used dynamic pressure to force air through the slots. However, the dynamic pressure acting on the slots increased the blade's profile drag. Other designs have been proposed in which the intake slots are not placed at the tip and dynamic pressure is not the means of accelerating that air. One such design placed the intake slots near the blade root, where dynamic pressure and drag are much lower. The air is pumped through along the blade length by the centrifugal forces acting along the rotating blade. Fig. 1.7 shows the centrifugal pumping slotted blade design. The centrifugal pumping design differs from the slotted tip design in that centrifugal force accelerates air out the tip slots, rather than high dynamic pressure. Watkins et al. [15, 16] examined active and passive flow and circulation control methods, while Lorber et al. [17] patented a passive flow control system which utilized centrifugal pumping. While all of these designs utilized centrifugal pumping, none were used as a method of vortex diffusion, and none involved flow field measurements at the rotor. Because the power penalty incurred by the slotted tip design resulted from the high drag and dynamic pressure at the blade tips, it was hypothesized that a centrifugal pumping blade could offer similar vortex diffusion characteristics while reducing or eliminating the performance penalty.

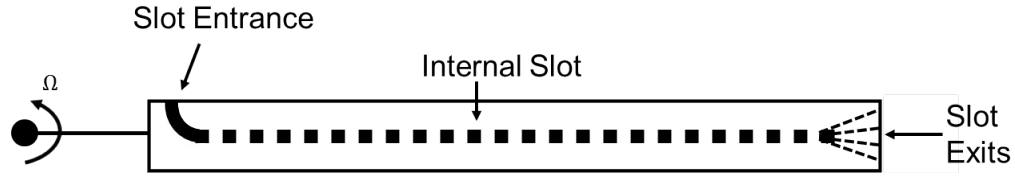


Fig. 1.7: The centrifugal pumping slotted blade design

## 1.5 Objectives

Brownout is a phenomenon caused by the interaction of a rotor wake with a sediment bed. The uplifted sediment cloud obstructs the pilot's view, harms equipment, and poses severe short- and long-term operational hazards. Previous work established that a rotor hovering in ground effect generates tip vortices which persist to older wake ages (Lee et al. [1]) when compared to a rotor operating out of ground effect. Johnson et al. [12] and Sydney et al. [3] showed that reintensified tip vortices were the primary cause of the mechanisms by which sediment is entrained into the flow. Milluzzo et al. [4] found that a slotted blade tip design significantly diffused tip vortices but incurred a power penalty. A potential solution to the power penalty was found in the work of Watkins et al. [15, 16] and Lorber et al. [17], who studied centrifugal pumping designs.

The previous work [1, 3, 12] demonstrated the importance of blade tip vortices as a cause of brownout, and Milluzzo et al. [4] showed that the slotted blade tip design significantly diffused the developing tip vortices. The current work aimed to determine the effectiveness of a pumping blade design in diffusing tip vortices. To that end, the project addressed four specific questions:

1. Does changing the position of the intake slot (i.e., moving it inward to create a

pumping blade rather than a slotted tip blade) provide the same level of tip vortex diffusion as that documented by Milluzzo et al. [4] in testing the slotted tip design with intakes at the end of the blades?

2. Does the orientation of the exit slots at the blade tip affect the rate of tip vortex diffusion?

3. Does changing the position of the intake slot (i.e., moving it to the blade root) reduce or eliminate the performance penalty associated with the slotted tip design tested by Milluzzo et al. [4]?

4. Does changing the orientation of the exit slots at the blade tip affect the performance of the rotor?

In order to answer these questions, four rotor blade designs, with intake slots near the hub and exit slots of varying orientation at the tip, were tested. Performance measurements determined the effect of the blade designs on rotor performance, while flow field measurements were taken to investigate the effect of the blade designs on vortex diffusion characteristics.

## 2. DESCRIPTION OF EXPERIMENT

The experiment was carried out using a teetering two-bladed rotor system with continuously variable collective blade pitch. Table 2.1 summarizes the rotor characteristics and test conditions. Fig. 2.1 shows the basic rotor test stand and ground plane setup. All rotor blades had a radius of 0.408 m (16 in) and a mean chord of 44.5 mm (1.752 in). The blades were untwisted with NACA 2415 airfoils throughout. The rotor was tested at a height of one rotor radius above the ground plane (i.e.,  $z/R = 1.0$ ) in order to simulate ground effect conditions, and it was mounted horizontally. The ground plane was circular with a diameter equal to four rotor radii and was painted a flat black to minimize surface reflections. Recirculation was minimized in the flow conditioned test cell by means of flow diverters along the surface of the ground plane and honeycombed flow conditioning screens mounted upstream of the rotor. As a result, measured turbulence levels of the incoming flow were reduced to under 1% of the flow velocities induced in the rotor wake. All four experimental blades and the baseline blade were tested under the same operating conditions. The blade loading coefficient,  $C_T/\sigma$ , was 0.08 for high thrust conditions and 0.0533 for low thrust conditions.  $C_T/\sigma$  was maintained for all rotor configurations as the value directly affected tip vortex strength. The rotor was operated at a frequency of 35 Hz (2,100 rpm), yielding a rotor tip speed of  $89.06 \text{ m s}^{-1}$  ( $292.21 \text{ ft s}^{-1}$ ), a nominal tip Mach number of 0.27, and a chord Reynolds number of 282,385. Tip Mach number was the

Table 2.1: Summary of rotor characteristics and test conditions

Blade Airfoil	NACA 2415
Number of Blades, $N_b$	2
Blade Radius, $R$	0.408 m
Mean Chord, $c$	44.5 mm
Rotational Frequency, $\Omega$	35 Hz
Rotor Tip Speed, $V_{tip}$	89.06 m/s
Rotor Height, $z/R$	1.0
Tip Mach Number, $M$	0.27
Tip Reynolds number, $Re$	282,385

ratio of tip speed to the speed of sound, while Reynolds number was the ratio of inertial forces to viscous forces in the flow.

## 2.1 Blade Tips

Five blade tip designs were used in the experiment: a baseline blade and four test variations. Baseline measurements were taken using a rectangular non-slotted blade. The four experimental designs featured an inlet slot near the hub. Internal slots connected the inlet slot to exit slots at the blade tip. The basic layout of a pumping blade design was depicted in Fig. 1.7. The four blade designs differed in the orientation at which air was expelled, with exit angles of  $0^\circ$ ,  $30^\circ$ ,  $45^\circ$ , and  $60^\circ$  above the plane intersecting the chord line of the blade. Fig. 2.2 defines the angle used to describe the orientation of the exit

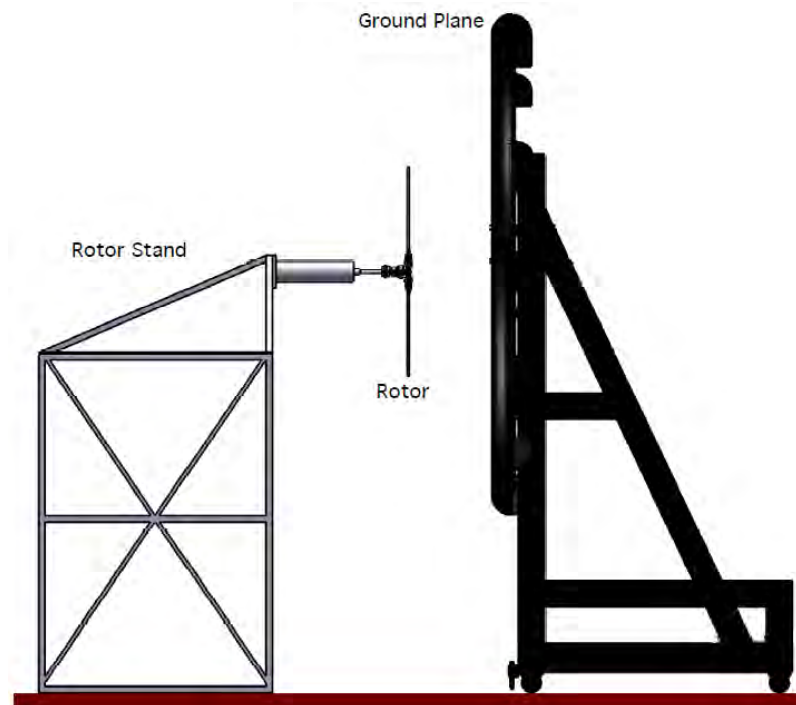


Fig. 2.1: Basic test setup [4]

slots at the blade tip. In the pumping blade designs, air entered the intake slot and was pumped along the length of the blade. The turbulent flow was ejected from the exit slots into the forming vortex core with the aim of increasing the rate of tip vortex diffusion. Dr. Dancilia of the University of Texas at Austin provided the pumping blades.

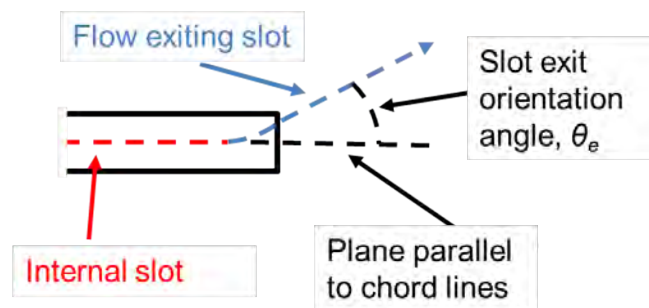


Fig. 2.2: Exit slot orientation

## 2.2 Theory

Several parameters are used to describe a rotor's operating conditions, as defined by Leishman [18]. The thrust,  $T$ , and power,  $P$ , produced by the rotor, are easily measured properties which describe rotor performance. As shown below, thrust and power can be converted to the non-dimensional coefficients of thrust and power,  $C_T$  and  $C_P$ .

$$C_T = \frac{T}{\rho A (\Omega R)^2} \quad (2.1)$$

$$C_P = \frac{T}{\rho A (\Omega R)^3} \quad (2.2)$$

In each equation,  $A$  is the rotor disk area (i.e., the area swept out by the rotor blades in the rotation of the rotor),  $\rho$  is air density,  $\Omega$  is the rotor's angular velocity, and  $R$  is the rotor's radius. Disk loading, a factor which affects downwash velocity, is obtained by dividing thrust by rotor disk area. Solidity,  $\sigma$ , is the area of the rotor blades as a fraction of disk area. The thrust coefficient and rotor solidity are used to calculate the blade loading coefficient,  $C_T/\sigma$ , a factor which is directly related to tip vortex strength. For this reason, maintaining a constant  $C_T/\sigma$  value was important in the current work, as it reduced the number of variables present in the test. Similarly, power loading,  $C_P/\sigma$ , is obtained from the power coefficient and the blade solidity.

According to momentum theory, a common mathematical model for describing rotor performance, a rotor's power can be attributed to two sources: induced power,  $C_{Pi}$ , is the power used to create rotor thrust, while profile power,  $C_{P0}$ , is required to overcome



the drag on the blades. This yields the following equations:

$$C_{P_i} = \frac{\kappa C_T^{3/2}}{\sqrt{2}} \quad (2.3)$$

$$C_{P_0} = \frac{\sigma C_{d_0}}{8} \quad (2.4)$$

$$C_P = C_{P_i} + C_{P_0} \quad (2.5)$$

Here,  $C_{d_0}$  is the average drag coefficient of the blades, determined by the airfoil type of the blades. The induced power factor,  $\kappa$ , accounts for non-ideal factors in the induced power, such as lift distribution and tip vortices. It is important in this work because the experimental blades differ only in their vortex diffusion characteristics, so that comparing the  $\kappa$  values of pumping blades and the baseline blade indicate their relative effectiveness in diffusing vortices.

The pumping blades also had a secondary source of thrust. The mass flow of air through the slots created a tip jet-like effect. When the slots were oriented, this produced a negative thrust effect,  $F_m$ , such that the measured thrust of the rotor was decreased. This thrust component was calculated to be a factor of mass flow rate, exit velocity, and slot orientation.

$$F_m = (\rho A_{exit} V_{exit}) V_{exit} \sin(\theta_{exit}) \quad (2.6)$$

$A_{exit}$  and  $V_{exit}$  were the cross sectional area and flow velocity at the exit slots, respectively, while  $\theta_{exit}$  was the exit slot orientation.

Finally, in describing the development of a rotor wake, phase and wake age must be defined. Phase is the angular position of the rotor blades relative to a reference position. When the phase reaches  $360^\circ$ , the rotor has undergone one complete revolution. Similarly, wake age,  $\zeta$ , describes the age of a flow structure in terms of phase. For example, the wake age of a tip vortex is determined by the angular displacement of the rotor since the vortex was created. Wake age is especially useful in describing flow fields and the development of tip vortices.

### 2.3 *Performance Measurements*

Performance measurements were acquired for each blade design to determine the thrust produced and power required for a range of collective angles. The measurements were obtained using a combination load and torque cell capable of resolving  $C_T$  to  $\pm 4.38 \times 10^{-6}$  and  $C_P$  to  $\pm 2.74 \times 10^{-7}$ . This resolution was achieved using signal conditioning and calibration. A performance sweep was performed for each blade, measuring the thrust and power of the rotor for a range of collective angles from  $-3^\circ$  to  $16^\circ$ . The performance curves could then be used to determine the collective pitch required to meet a given operating condition, such as a specific blade loading coefficient. Ambient pressure and temperature were also recorded so that atmospheric effects could be factored out of the performance data.

## 2.4 *Flow Field Measurements*

The experiment used high resolution flow visualization (FV) to qualitatively analyze the flow and particle image velocimetry (PIV) to provide quantitative measurements. The experimental setup is shown in Fig. 2.3. The setup used a Nd:YAG laser which emitted light at a wavelength of 532 nm, in 200 mJ pulses at a frequency of up to 15 Hz. To take flow field measurements, a high energy laser beam was reflected from a mirror and through convex and spherical lenses so that it diverged into a sheet, illuminating a plane in the rotor wake. The sheet was normal to the rotor tip path plane. The spherical lens narrowed the waist of the laser sheet to 2 mm, increasing its intensity. The laser sheet illuminated seed particles within the flow, creating visible markers in the flow. In FV, the tracer particles were thick enough that flow structures could be visualized in a single image. The image of the illuminated particles was captured by an 11 MP CCD camera oriented with its imaging axis orthogonal to the laser sheet and focused on a particular region of interest (ROI). The laser and camera were synchronized such that the laser pulse straddled the camera images. All images were phase resolved, i.e., sequential images recorded the wake at the same rotor phase. This allows the wake to be examined for a specific rotor phase (e.g., analyzing tip vortices at a given wake age). However, individual flow structures cannot be tracked as they develop in phase-resolved measurements. Seven configurations were tested to obtain flow field measurements: each of the five blade designs was tested at a high thrust condition, and the baseline blade and  $0^\circ$  exit slot pumping blade were also tested at a low thrust condition.

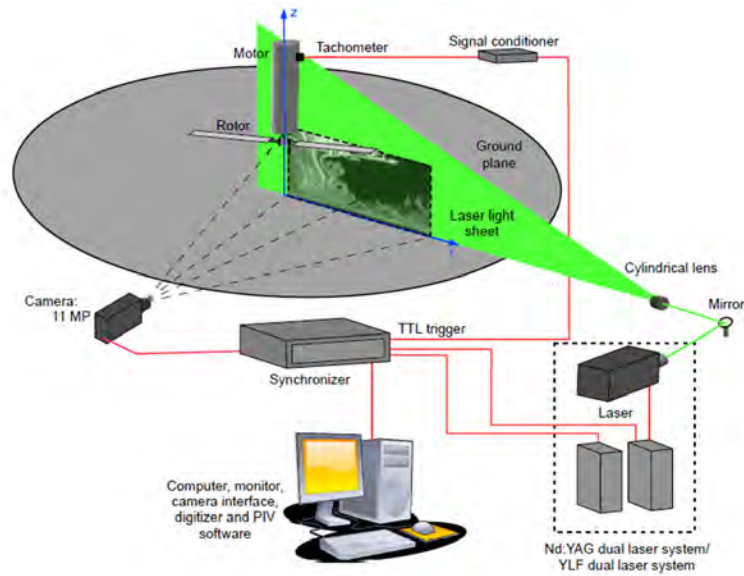


Fig. 2.3: The test setup for flow field measurements [2]

#### 2.4.1 PIV Imaging

Particle image velocimetry (PIV) is a technique used to measure flow velocity at a given instant in a particular region of interest. Submicron tracer particles were seeded into the airflow and illuminated by the laser sheet. The camera recorded two sequential images, with a pulse separation time,  $\Delta t$ , separating the two images. The pulse separation time ranged from 1.5 to 6  $\mu s$ , depending on the ROI used. The two images formed a pair, and each image was split into a number of interrogation windows. Each interrogation window had base-2 dimensions, such as 16x16 or 32x32 pixels. Within each interrogation window, the average particle displacement between the images was determined. Using this displacement and the pulse separation time, a velocity vector was determined for each interrogation window. Combining all calculated velocity vectors yielded a velocity field which could then be analyzed to examine characteristics of the rotor wake, such as

the vorticity of the tip vortices.

Fig. 2.4 shows the two regions of interest (ROIs) used in the experiment. ROIs 1 and 2 provided sufficient spatial resolution over the entire field of interest. Because the experiment used a two bladed rotor, flow field measurements were recorded at wake ages up to  $180^\circ$ , at which point another blade passed through the laser sheet, making the  $180^\circ$  wake age measurement the same as a  $0^\circ$  wake age measurement. To fully resolve the wake, six wake ages were chosen in increments of  $30^\circ$  from  $0^\circ$  to  $150^\circ$ . In each ROI, 550 images were recorded for each blade configuration tested at each wake age. The PIV processing used a 16-by-16 pixel window size with a 75% overlap, effectively yielding one velocity vector for every 4-by-4 pixel area. This high resolution was required to resolve the steep velocity gradients in the rotor wake. Additionally, the interrogation windows of the second window were translated and deformed to maximize the number of particles tracked, increasing the accuracy of the velocity measurements. Images were validated through a local median test of the 3-by-3 neighboring vectors, with images with more than 5% spurious vectors being discarded, although in practice few of these cases occurred.

Pulse separation was chosen so that the particle displacement in an image pair was greater than the particle's diameter but less than 1/4th the side length of the interrogation area. Pulse separation time was also minimized to reduce the curvature error resulting from particles following a curved path within the flow (and especially in tip vortices). This also minimized acceleration error, in which an accelerating particle in unsteady flow was assumed to have constant velocity. With these criteria in mind, the pulse separation time was  $6 \mu\text{s}$ . These measurements were chosen in order to maximize accuracy and

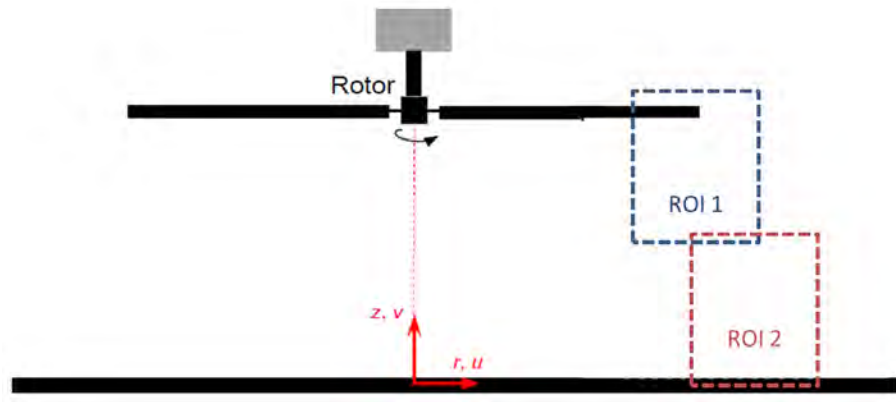


Fig. 2.4: The two regions of interest (ROIs) examined in the experiment

optimize the PIV measurements obtained.

## 2.5 Data Analysis

Raw performance data yielded thrust and power measurements for a range of collective angles. These measurements were non-dimensionalized, and a least squares fit curve was used to fit a modified momentum theory model to the measured data. As a predictive model, this was then used to calculate the collective angle required to obtain a given thrust output for a given blade design. Additionally, the model was analyzed to examine the performance of each blade type through a range of thrust conditions, and the induced power factor of each blade design was calculated to determine the initial vortex diffusion characteristics of each blade design.

In addition to the performance curves, flow visualization data also offered a qualitative analysis of the vortex diffusion characteristics of each blade. Absolute velocity contours obtained from PIV data allowed the flow field to be analyzed for swirl velocities of tip vortices. This allowed another qualitative comparison of the merits of various blade

designs. The data analysis process is discussed more in depth in the following section.

### 3. RESULTS

#### 3.1 *Performance Results*

Performance measurements were taken to determine the thrust produced and power required for each blade design. Fig. 3.1 shows the power loading coefficient,  $C_P/\sigma$ , versus blade loading coefficient,  $C_T/\sigma$ , for each rotor configuration. The exit slots increased the blades' profile drag, so when the rotors were operated at lower thrust conditions (where profile losses dominate), the pumping blade designs required more power than the baseline blade. However, as the thrust produced by the rotors was increased, the power requirements of the pumping blade designs approached that of the baseline blade. This occurred because the pumping blade designs experienced a lower induced power requirement than the baseline blade. Because the baseline and pumping blade designs had identical twist rates (i.e., untwisted) and planforms (i.e., constant blade chord), the differences in induced power requirement were caused by differences in the initial diffusion of the tip vortex convected by the blades.

To characterize the induced power differences between the pumping blade designs and the baseline blade, the induced power factor,  $\kappa$ , was determined. The induced power factor was determined using a least-squares fit of modified momentum theory to the measured performance data shown in Fig. 3.1. The induced power factors for each rotor are



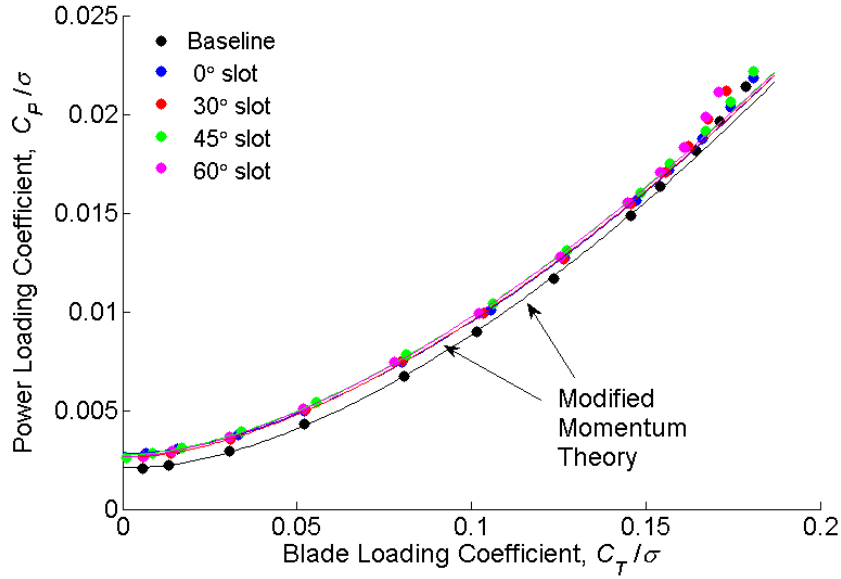


Fig. 3.1: Plot of the measured power polar for each rotor.

shown in Table 3.1. While the  $0^\circ$  pumping blade design was found to have the lowest induced power factor (approximately 1.7% lower than that of the baseline blade), the  $30^\circ$ ,  $45^\circ$ , and  $60^\circ$  pumping blade designs had induced power factors approximately equal to or slightly greater than the baseline blade.

The degraded performance of  $30^\circ$ ,  $45^\circ$ , and  $60^\circ$  pumping blade designs compared to the  $0^\circ$  design can be explained using conservation of momentum, i.e., the mass flow rate of the air out of the exit slots generated a force that opposed the rotor thrust or a created negative thrust effect ( $F_{in}$ ). The negative thrust was determined to be a function of the mass flow rate of air through the slots, the air's exit velocity, and the orientation of the exit slots. The negative thrust effect was calculated assuming no viscous losses in the slots (i.e., the exit velocity of the air was equal to the rotor's tip speed), and the air density, exit slot area and orientation were known. Removing the negative thrust effects from the measured performance data, an adjusted induced power factor could be determined for

Table 3.1: Force generated by mass flow and normalized induced power factor for the four pumping blade designs

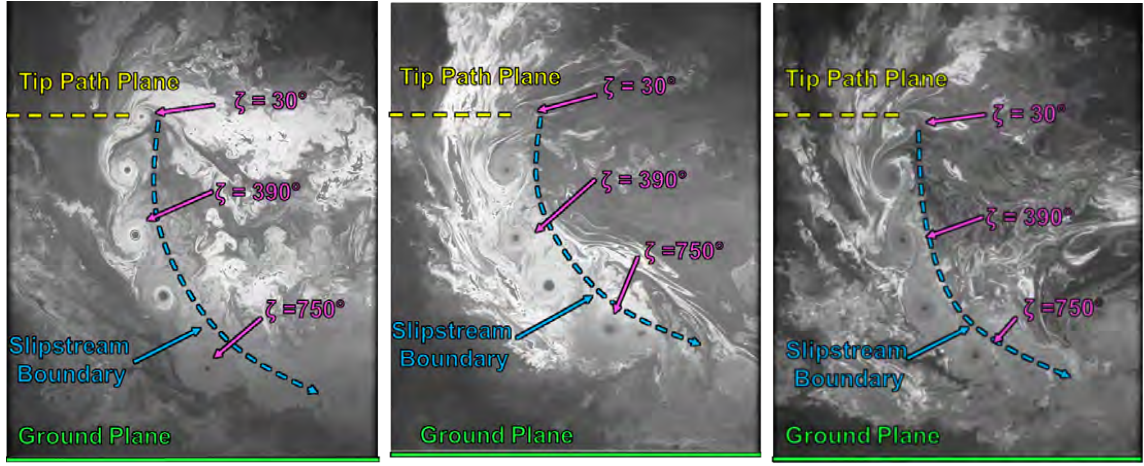
Exit Slot Orientation	$F_{\dot{m}}$	$\kappa_{\text{Unadjusted}} / \kappa_{\text{Baseline}}$	$\kappa_{\text{Adjusted}} / \kappa_{\text{Baseline}}$
0°	0.0000	0.9830	0.9830
30°	-0.2211	0.9966	0.9854
45°	-0.3127	1.0044	0.9893
60°	-0.3830	1.0049	0.9855

the 30°, 45°, and 60° pumping blade designs. Table 3.1 shows that when the effects of the negative thrust were removed, the adjusted induced power factors,  $\kappa_{\text{adjusted}}$  for all pumping blades were similar, to within 1%.

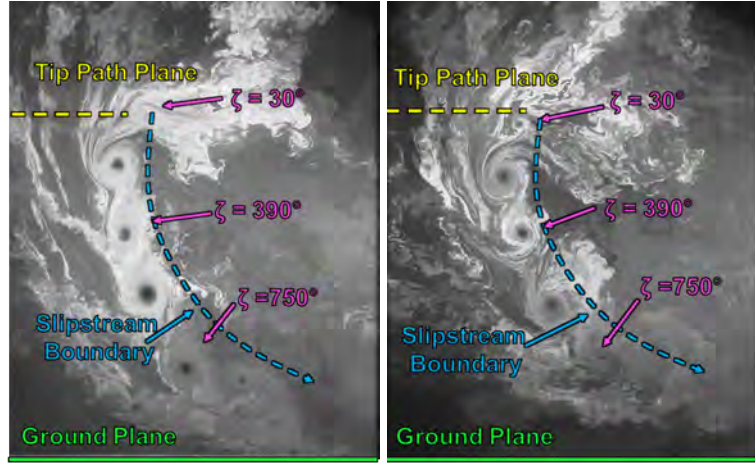
### 3.2 Flow Visualization

Flow visualization was performed to qualitatively highlight the primary flow structures in the wake. Seed particles were judiciously introduced into the flow in concentrated bands, allowing the laser to illuminate the flow structures. Fig. 3.2 shows representative flow visualization images of each blade design with the reference blade at azimuth angle  $\psi_b = 30^\circ$  and the rotor operating in ground effect with a blade loading coefficient of  $C_T/\sigma = 0.08$ . Therefore, the image depicts tip vortices of wake ages  $\zeta = 30^\circ, 210^\circ, 390^\circ$ , etc.

The FV results showed that the baseline and pumping blades produced qualitatively similar flow fields. Each blade trailed a tip vortex, which in the image is distinguished



(a) Baseline non-pumping blade (b)  $0^\circ$  exit slot orientation (c)  $30^\circ$  exit slot orientation



(d)  $45^\circ$  exit slot orientation (e)  $60^\circ$  exit slot orientation

Fig. 3.2: Representative flow visualization with the reference blade at a blade azimuth angle  $\psi_b$  of  $30^\circ$  and the rotor operating at a  $C_T/\sigma = 0.080$ , for the: (a) Baseline non-pumping blade (b)  $0^\circ$  exit slot orientation, (c)  $30^\circ$  exit slot orientation, (d)  $45^\circ$  exit slot orientation, and (e) the  $60^\circ$  exit slot orientation.

by a dark circular region, called a seed void (so called because the darkness is a result of a lack of illuminated seed particles in the region). The seed voids develop because centrifugal and Coriolis accelerations act on the seed particles to accelerate them outward from the vortex core. It is important to note that because each image is seeded differently, apparent differences in the dimensions of tip vortices in the images do not necessarily reflect differences in vortex strength or flow structures.

Although the size of a seed void does not necessarily indicate the relative strength of a vortex, the formation of a dark region, which is dependent solely on sufficient centrifugal and Coriolis forces, is indicative of vortex formation. The FV images show that the baseline blade design shed vortices which rolled up very quickly, forming as early as a wake age of  $\zeta = 3^{circ}$ . In contrast, no such clear seed void appears for any of the pumping blades at  $\zeta = 30^{circ}$ ; see Fig. 3.2. This difference indicated that the pumping blades produced tip vortices that were initially more diffused than those generated by the baseline blade design. Initial diffusion of the tip vortex would be expected to lower a blade's induced power requirements, so this observation supported the performance results previously discussed.

However, while the pumping blades initially diffused the tip vortices, they did not completely diffuse them. Rather, Fig. 3.2 clearly shows that mature vortices with laminar (i.e., smooth) core flow structures were formed by a wake age of  $\zeta = 210^{circ}$ . The FV images indicate that the initial diffusion of the tip vortices by the pumping blade designs was not sufficient to prevent vortex reintensification in ground effect. Laminar flow in the vortex core is one main causes of tip vortices which persist to later wake ages. In laminar flow, vortex diffusion occurs due to shear stresses on the molecules in the flow,

while in turbulent flow, diffusion occurs on a larger scale. The FV images show that the tip vortices generated by the pumping blades overcame their initial diffusion and rolled up as the wake expanded along the ground plane. Fig. 3.2 shows that for each blade, the tip vortices persisted to wake ages as old as three to four rotor revolutions.

Additional measurements were performed at a lower blade loading coefficient of  $C_T/\sigma = 0.053$  in order to examine the effect of mass flow rate on the tip vortex diffusion. These measurements were performed on the baseline and  $0^\circ$  pumping blades. Figures 3.3 and 3.4 show representative FV images, with the reference blade position of  $\psi_b = 30^\circ$ , for the baseline and  $0^\circ$  pumping blade, respectively, at each operating condition. The baseline blade generated a similar flow field in each case, trailing tip vortices that rolled up almost immediately and persisted to the ground plane. In contrast, when the  $0^\circ$  pumping blade was operated at the lower blade loading condition, it trailed significantly more diffused tip vortices, as shown by the lack of clear seed voids in Fig. 3.4a. The weaker vortices produced at low thrust did not appear to overcome the initial diffusion, as no coherent vortices were observed near the ground. This result suggested that an increased mass flow rate of air through the pumping slots may be required to diffuse stronger tip vortices produced in higher thrust conditions.

### 3.3 *Instantaneous Flow Field Measurements*

Figure 3.5 shows representative contours of the instantaneous vorticity, at a reference blade position of  $\psi_b = 30^\circ$ , for each blade set operating at  $C_T/\sigma = 0.08$ . All blade sets produced tip vortices that induced local regions of relatively high vorticity (i.e., greater

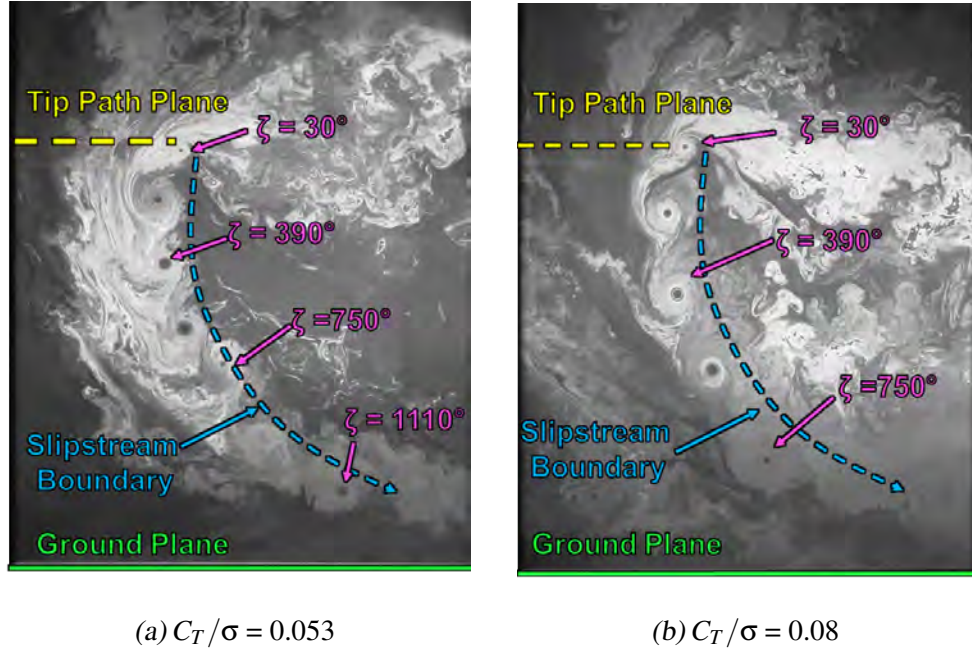


Fig. 3.3: Representative flow visualization of the baseline blade for each operating condition at  $\psi_b = 30^\circ$ : (a)  $C_T/\sigma = 0.053$ ; (b)  $C_T/\sigma = 0.080$ .

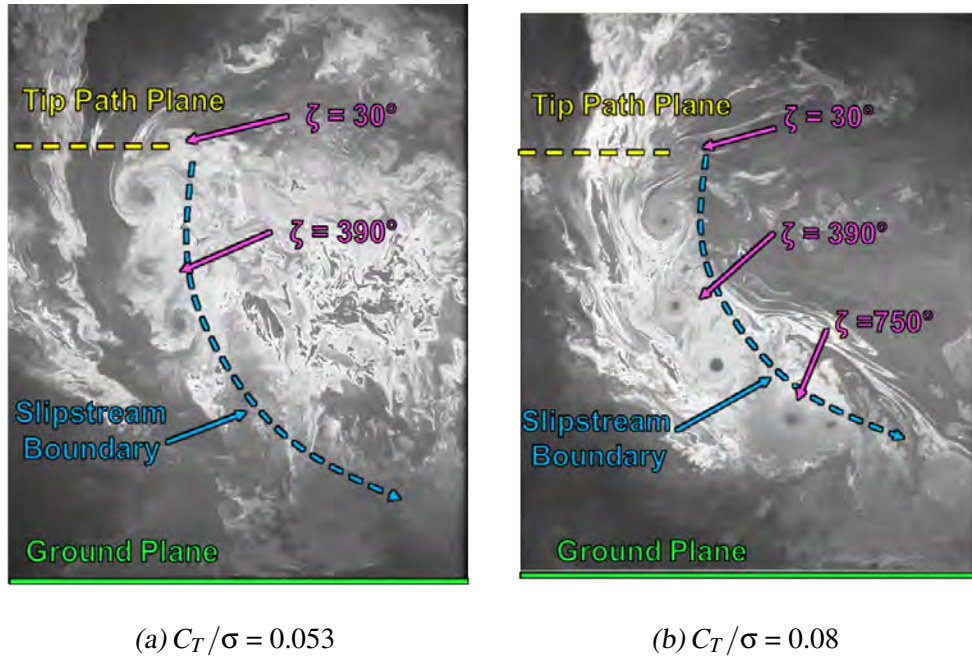


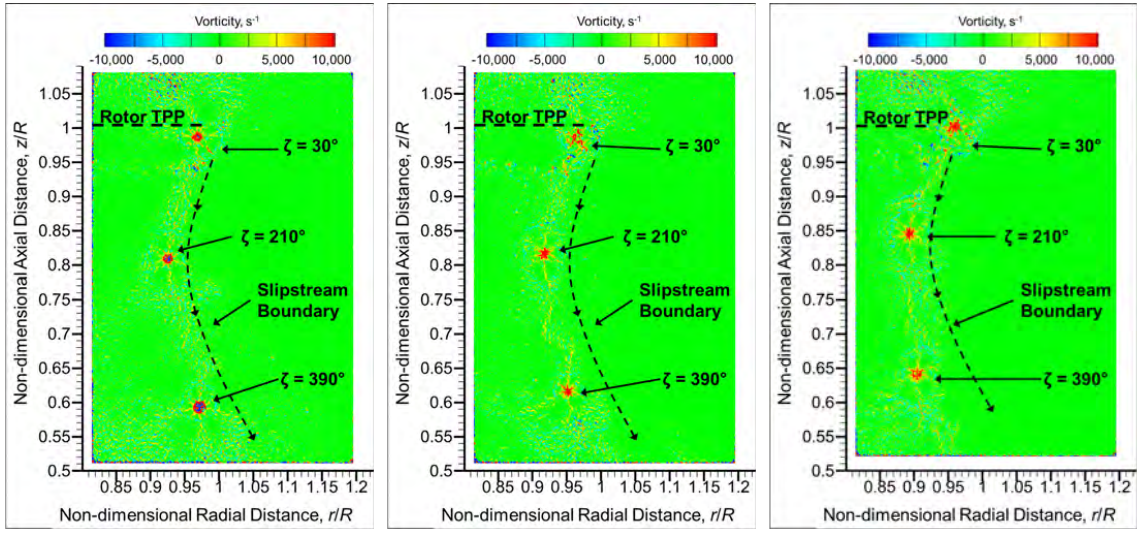
Fig. 3.4: Representative flow visualization of the  $0^\circ$  pumping blade for each operating condition at  $\psi_b = 30^\circ$ : (a)  $C_T/\sigma = 0.053$ ; (b)  $C_T/\sigma = 0.080$ .

than  $10000 \text{ s}^{-1}$ ). The baseline blade produced tip vortices that were immediately very concentrated, while the vorticity plots show that the pumping blades, and the  $0^\circ$  pumping blade in particular, produced tip vortices that were initially more diffused. However, the tip vortices overcame the initial diffusion, and at older wake ages (i.e.,  $\zeta = 390^\circ$ ), the tip vortices of the pumping blade designs overcame the initial diffusion and resembled those generated by the baseline blade. Concentrated regions of relatively high vorticity corresponded to tip vortices that generated relatively high locally induced swirl velocities; see Fig. 3.6. All blade sets produced tip vortices that induced local swirl velocities greater than 20% of the blade tip speed. The tip vortices generated by the baseline blade were significantly more coherent than those produced by the pumping blades, with larger regions of high induced velocity (i.e., greater than 20% of the tip speed). This difference between the tip vortices trailed by the baseline and pumping blades persisted to relatively older wake ages (i.e.,  $\zeta = 390^\circ$ ); see Fig. 3.6.

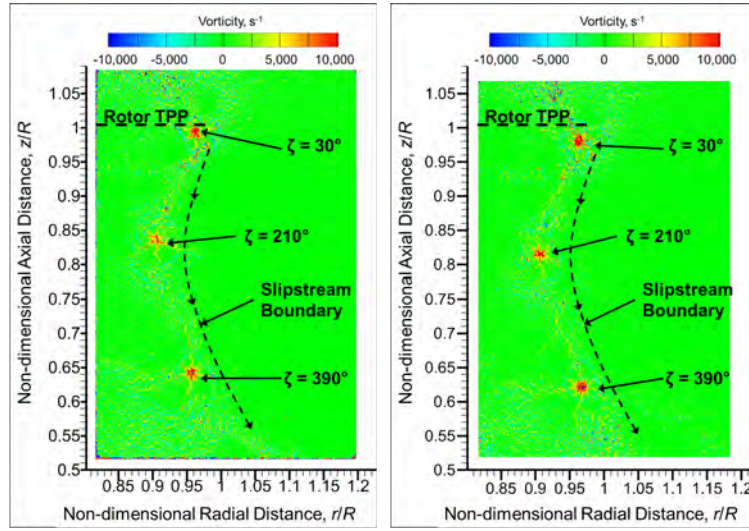
Figure 3.6 shows that at relatively early wake ages (i.e.,  $\zeta = 30^\circ$ ), the  $0^\circ$  and  $30^\circ$  pumping blades most successfully diffused the tip vortices, while the  $45^\circ$  and  $60^\circ$  pumping blades produced tip vortices slightly more diffused than those generated by the baseline blade. At relatively older wake ages (i.e.,  $\zeta = 390^\circ$ ), the tip vortices rolled up and reintensified as the rotor wake began to expand, and the tip vortices produced by all pumping blade designs appeared largely the same. The tip vortices produced by the pumping blades were more diffused than those of the baseline blade, but they still induced relatively high swirl velocities.

The flow fields generated by the baseline blade at lower and higher thrust conditions were qualitatively similar, as shown in Fig. 3.3. The rotor produced concentrated tip





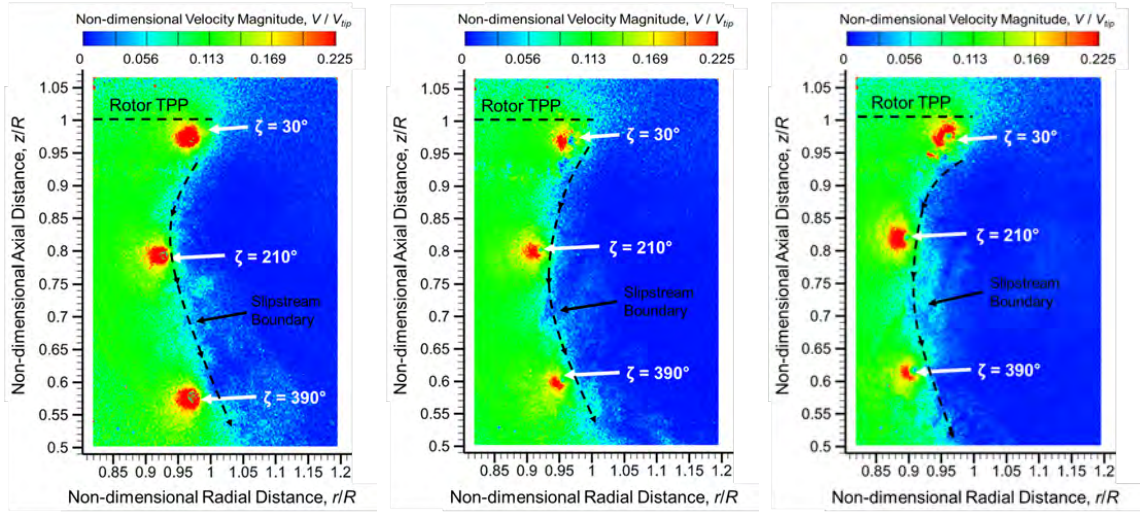
(a) Baseline non-pumping blade      (b) 0° exit slot orientation      (c) 30° exit slot orientation



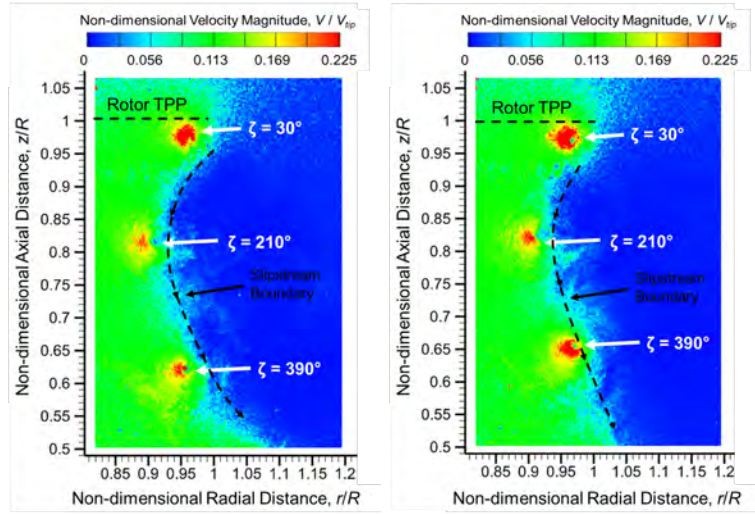
(d) 45° exit slot orientation      (e) 60° exit slot orientation

Fig. 3.5: Contours of instantaneous vorticity in ROI 1, with the reference blade at a blade azimuth angle  $\psi_b$  of  $30^\circ$  and the rotor operating at a  $C_T/\sigma = 0.080$ , for the: (a) Baseline non-pumping blade; (b)  $0^\circ$  exit slot orientation; (c)  $30^\circ$  exit slot orientation; (d)  $45^\circ$  exit slot orientation; and (e) the  $60^\circ$  exit slot orientation.





(a) Baseline non-pumping blade      (b)  $0^\circ$  exit slot orientation      (c)  $30^\circ$  exit slot orientation



(d)  $45^\circ$  exit slot orientation      (e)  $60^\circ$  exit slot orientation

Fig. 3.6: Contours of non-dimensionalized total velocity in ROI 1, with the reference blade at a blade azimuth angle  $\psi_b$  of  $30^\circ$  and the rotor operating at a  $C_T/\sigma = 0.080$ , for the: (a) Baseline non-pumping blade; (b)  $0^\circ$  exit slot orientation; (c)  $30^\circ$  exit slot orientation; (d)  $45^\circ$  exit slot orientation; and (e) the  $60^\circ$  exit slot orientation.

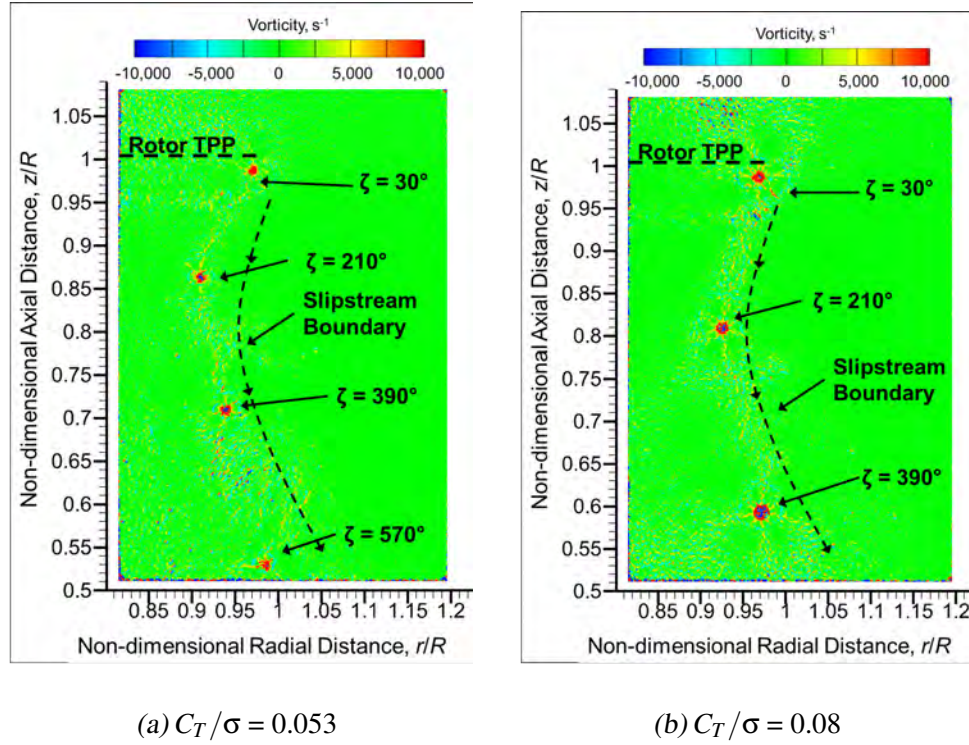


Fig. 3.7: Contours of instantaneous vorticity in ROI 1, for the rotor with the baseline blades at  $\psi_b = 30^\circ$  for each operating condition: (a)  $C_T/\sigma = 0.053$ ; (b)  $C_T/\sigma = 0.080$ .

vortices that persisted to older wake ages; see Figs. 3.7 and 3.8. Landegrebe [19–22] and Milluzzo and Leishman [23] noted that an increase in rotor thrust increased the downwash velocity in the wake. This was observed in the PIV images, where the tip vortices convected in the wake more quickly at the high thrust condition. Additionally, the higher blade loading at the high thrust condition resulted in stronger tip vortices with larger regions of high vorticity and locally high induced velocities, as would be expected.

Because the pumping blades, at the high thrust condition, did not effectively diffuse the tip vortices such that they did not reintensify, an examination of the effect of mass flow rate through the pumping slots on vortex diffusion was of particular interest. Increased mass flow rate was simulated by reducing the blade loading coefficient to

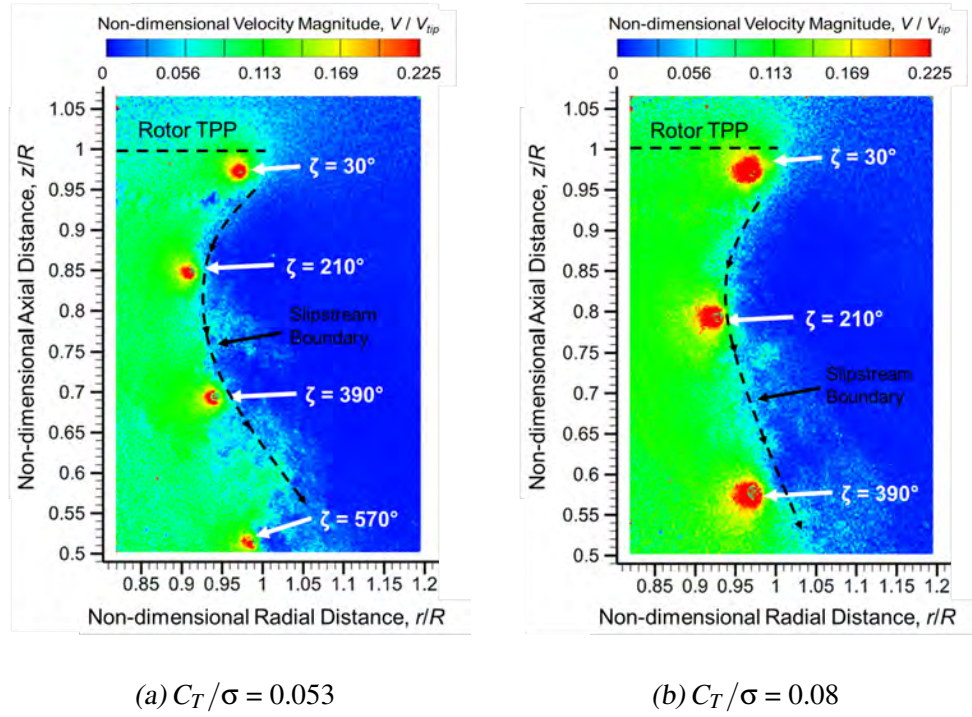


Fig. 3.8: Contours of non-dimensionalized total velocity in ROI 1, for the rotor with the baseline blades at  $\psi_b = 30^\circ$  for each operating condition: (a)  $C_T/\sigma = 0.053$ ; (b)  $C_T/\sigma = 0.080$ .

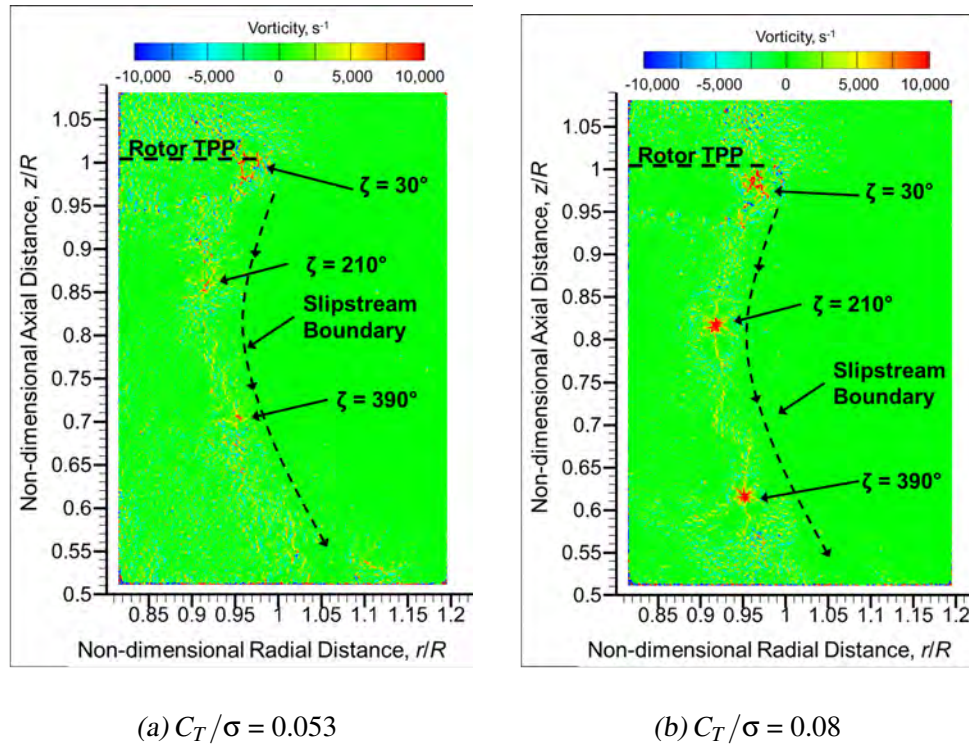


Fig. 3.9: Contours of non-dimensionalized total velocity in ROI 1, for the rotor with the  $0^\circ$  pumping blades at  $\psi_b = 30^\circ$  for each operating condition: (a)  $C_T/\sigma = 0.053$ ; (b)  $C_T/\sigma = 0.080$ .



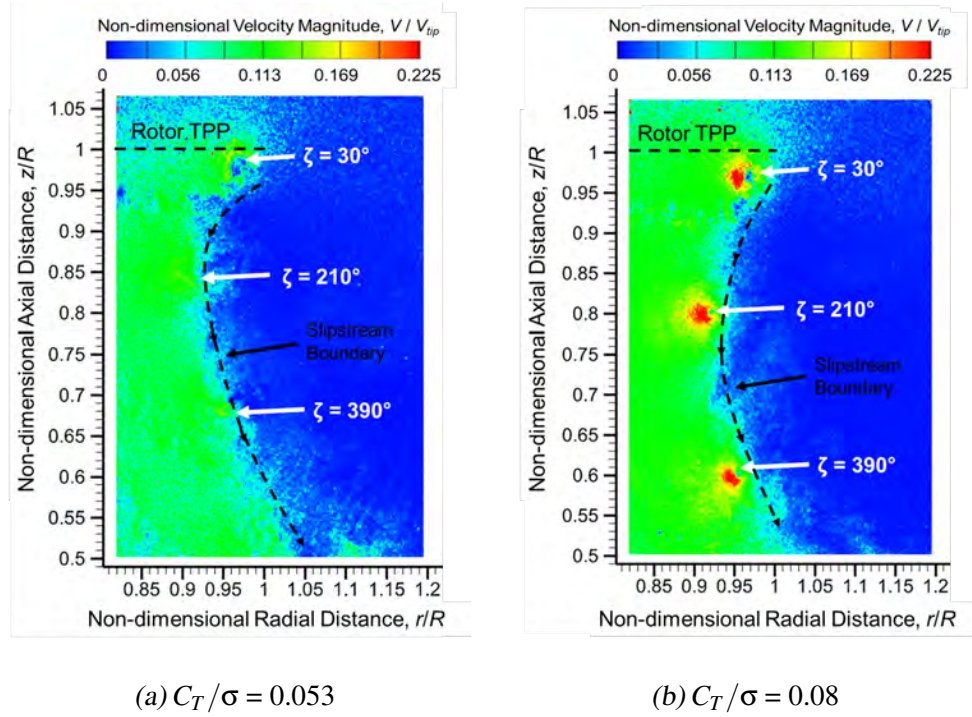


Fig. 3.10: Contours of non-dimensionalized total velocity in ROI 1, for the rotor with the  $0^\circ$  pumping blades at  $\psi_b = 30^\circ$  for each operating condition: (a)  $C_T/\sigma = 0.053$ ; (b)  $C_T/\sigma = 0.080$ .

$C_T/\sigma = 0.053$ . Figures 3.7 and 3.9 show representative contours of instantaneous vorticity for the baseline and  $0^\circ$  pumping blade designs, respectively, at higher and lower blade loading coefficients, while Figs. 3.8 and 3.10 show instantaneous total velocity for the same conditions. Notably, the flow fields generated by the pumping blade differed greatly when the thrust conditions were altered. Figures 3.9a and 3.10a show that at low thrust, the pumping blade produced relatively diffused vortices. The tip vortices generated by the pumping blade design at the lower thrust condition created diffused regions of relatively low vorticity. Similarly, the swirl velocities induced by the tip vortices were significantly lower than at high blade loading, and the induced swirl velocities were close to the downwash velocities in the rotor wake. Furthermore, at low thrust, the pumping blades did not merely prolong vortex rollup, as was observed with pumping blades at high thrust, but actually completely diffused vortices so that they did not reintensify, even at older wake ages (i.e.,  $\zeta \geq 30^\circ$ ). As previously discussed, because the  $0^\circ$  pumping blade successfully diffused the tip vortices at lower thrust conditions, it is expected that increasing the mass flow through the pumping slots would be required to diffuse the stronger tip vortices produced at higher thrust conditions.

In addition to instantaneous flow fields, the tip vortices were also analyzed using swirl velocity profiles. Figure 3.11 show the schematic for a swirl velocity profile, in which a cut is made across the vortex, and swirl velocity is plotted across the cut. The swirl velocity profile indicates both the peak swirl velocities and the position of the vortex core. A series of phase averaged swirl velocity profiles were plotted for each wake age so that the development and evolution of the tip vortices could be examined.

Figures 3.12 and 3.13 compare the swirl velocity profiles generated by the baseline

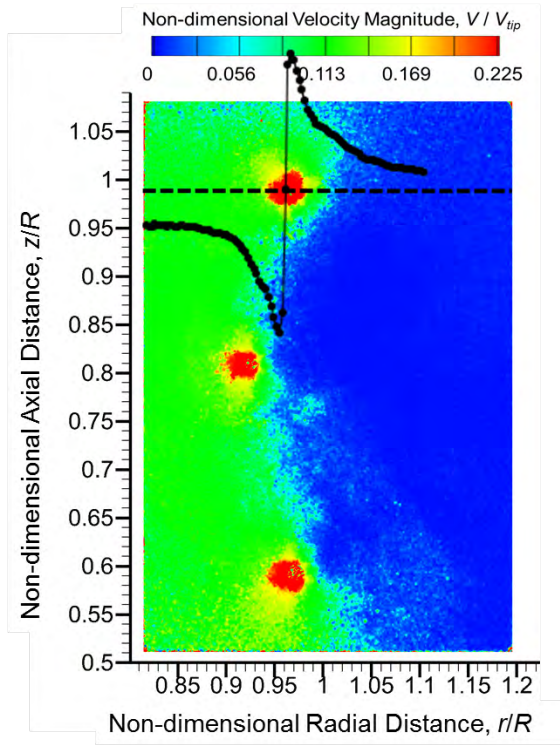


Fig. 3.11: Representative swirl velocity profile plotted across a tip vortex

and  $0^\circ$  pumping blades at earlier and later wake ages, respectively. Initially, the pumping blade generated tip vortices that were much more diffused than those produced by the baseline blade, with the latter blade inducing peak swirl velocities approximately 2.5 times those of the former; see Fig. 3.12. Despite the initial diffusion, however, the peak swirl velocities induced by the pumping blade remained relatively constant as the tip vortices aged, indicating that the tip vortices failed to diffuse. This lack of diffusion was much more apparent at older wake ages, where the swirl velocity profiles generated by the baseline and pumping blades were relatively similar, as shown in Fig. 3.13.

At the lower thrust condition, the vortices shed by the baseline and pumping blades differed much more significantly. Figures 3.14 and 3.15 show the swirl velocity profiles of tip vortices generated by the baseline and  $0^\circ$  pumping blade at  $C_T/\sigma = 0.053$ . In the

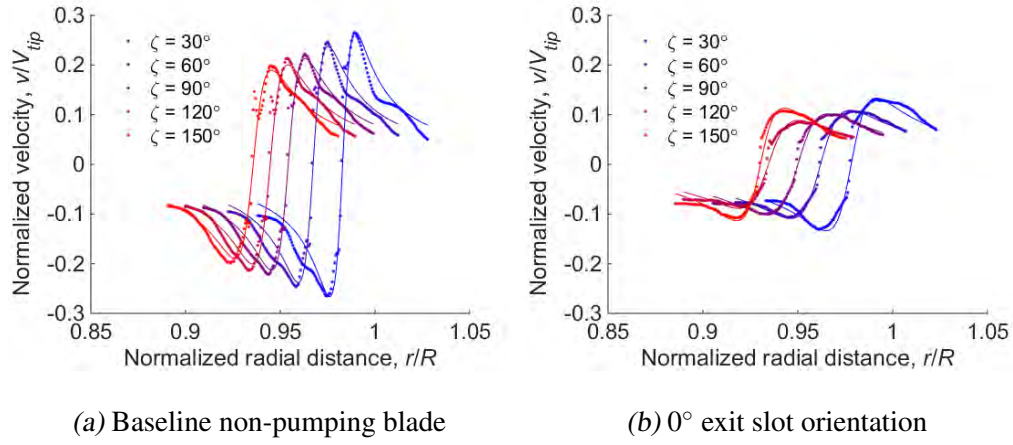


Fig. 3.12: Swirl velocity profiles at early wake ages ( $\zeta \leq 150^\circ$ ) operating at  $C_T/\sigma = 0.08$  for (a) the baseline blade and (b) the  $0^\circ$  pumping blade.

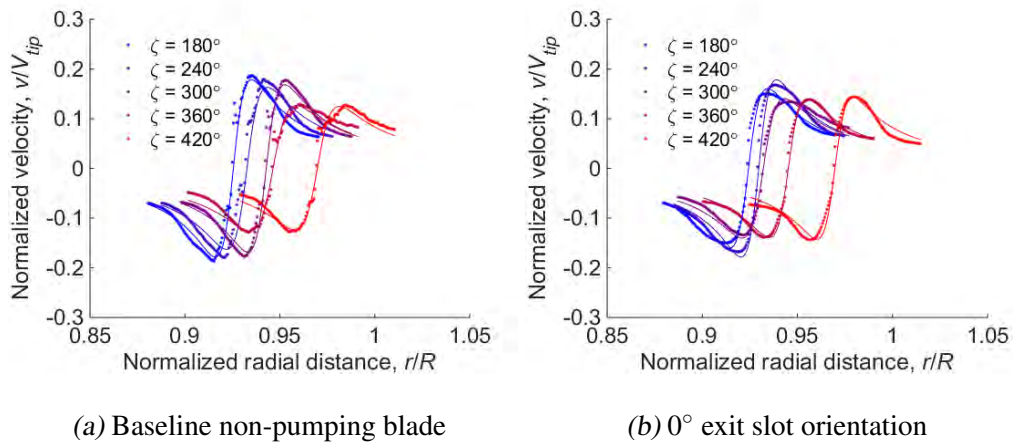


Fig. 3.13: Swirl velocity profiles at later wake ages ( $\zeta \geq 180^\circ$ ) operating at  $C_T/\sigma = 0.08$  for (a) the baseline blade and (b) the  $0^\circ$  pumping blade.



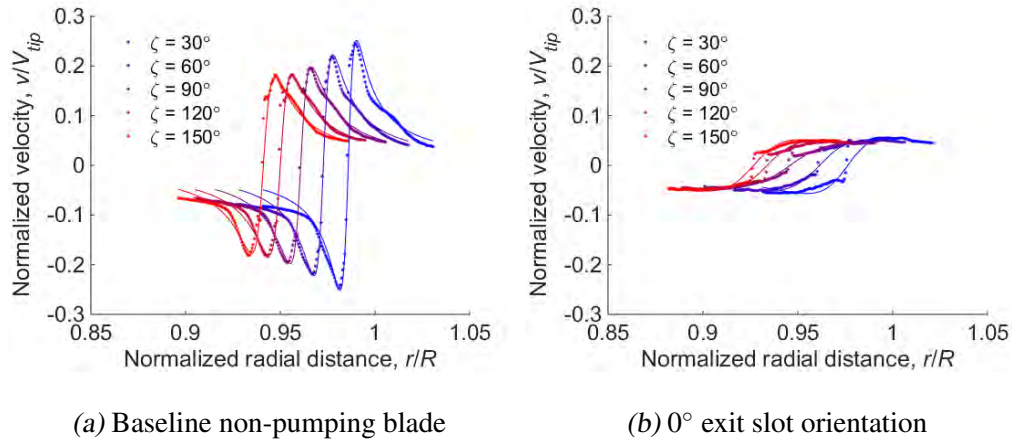


Fig. 3.14: Swirl velocity profiles at early wake ages ( $\zeta \leq 150^\circ$ ) operating at  $C_T/\sigma = 0.053$  for (a) the baseline blade and (b) the  $0^\circ$  pumping blade.

case of the baseline blade, the tip vortices were similar in both thrust cases. Specifically, the swirl velocity profiles showed relatively high peak swirl velocities and steep velocity gradients. However, the pumping blade produced diffused tip vortices with lower peak swirl velocities (approximately 20% those generated by the baseline blade) and relatively shallow velocity gradients. The vortices remained diffused, showing no signs of re-intensification at the older wake ages; see Fig. 3.15. Therefore, the swirl velocity profiles confirmed that at high thrust, the pumping blade generated tip vortices that were initially diffused, but did not diffuse completely, while at low thrust the pumping blade generated tip vortices that remained significantly diffused at older wake ages.

Understanding the initial behavior of the flow trailed by the rotor blades is necessary to explaining the behavior of the near-wall flow field (i.e., the flow near the ground plane). However, brownout is caused by the flow near the ground, where interaction between the rotor wake and the ground plane drives the uplift of sediment particles. Previous research

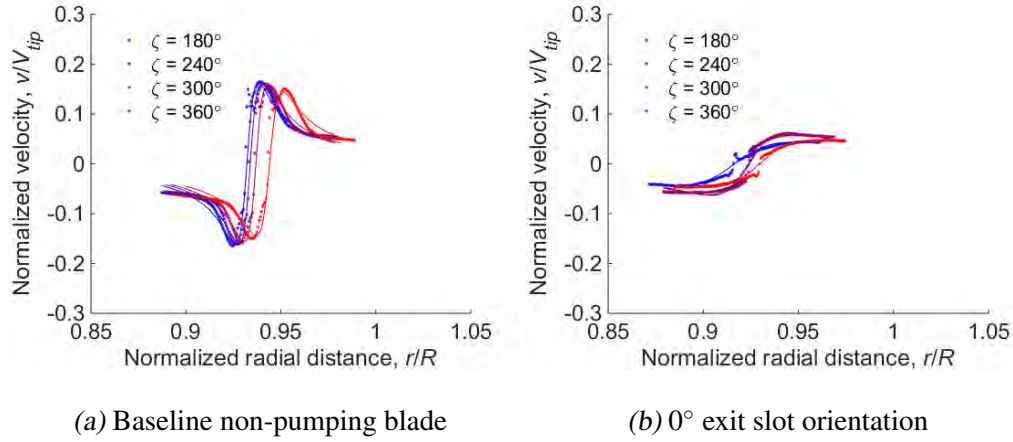


Fig. 3.15: Swirl velocity profiles at later wake ages ( $\zeta \geq 180^\circ$ ) operating at  $C_T/\sigma = 0.053$  for (a) the baseline blade and (b) the  $0^\circ$  pumping blade.

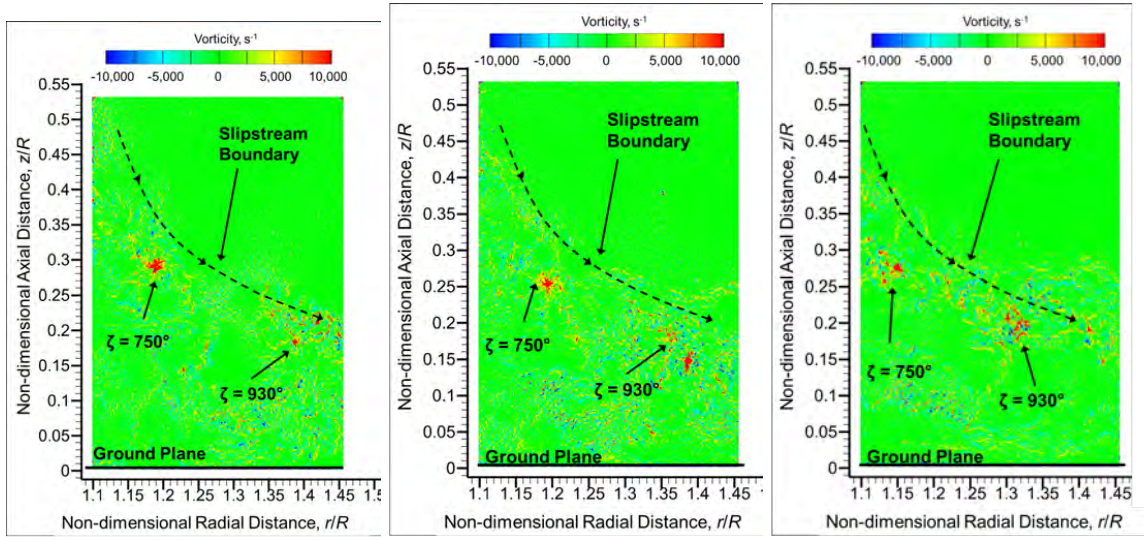
has shown that the interaction of the tip vortices near the ground with the sediment bed and the saltation layer drive the generation of the brownout cloud. In particular, the upwash velocities induced by the tip vortices entrain sediment particles into the flow and uplift them to become suspended in the air around the rotor. Therefore, the axial, or wall-normal, velocities induced by the tip vortices were studied in ROI 2, as these velocities most directly contribute to the formation of the brownout cloud.

Figure 3.16 shows representative contours of the instantaneous vorticity near the ground at a blade loading coefficient of  $C_T/\sigma = 0.08$  and a reference blade position of  $\zeta \geq 30^\circ$ . In all cases, the tip vortices near the ground showed similar regions of high vorticity, suggesting that the strength and concentration of the tip vortices was maintained as they approached the ground plane. Figure 3.17 shows representative contours of the instantaneous wall-normal velocity under the same operating conditions. While the pumping blades generated lower induced velocities near the rotor, as shown in ROI 1,

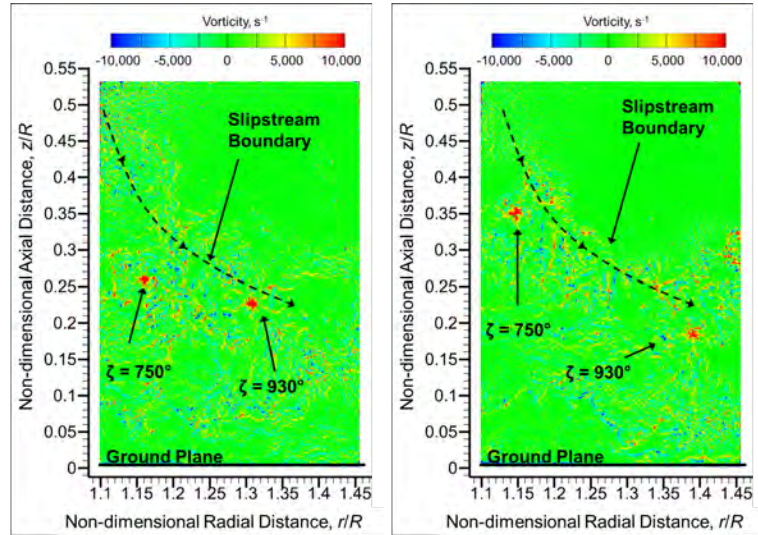
all blade sets induced similar velocities near the ground. Each blade set produced tip vortices with large regions of relatively high velocity upwash. These regions of upwash would have the potential to uplift significant amounts of sediment, thereby generating a brownout cloud.

Just as Fig. 3.7 showed that the baseline blade generated similar flow fields at high and low blade loading coefficients (i.e.,  $C_T/\sigma = 0.08$  and  $C_T/\sigma = 0.053$ , respectively) near the rotor, Fig. 3.18 shows that these similarities continued to the ground plane, in ROI 2. Specifically, tip vortices persisted to the ground, where they continued to exhibit similar concentrations of relatively high vorticity. Figure 3.19 showed that the tip vortices induced relatively high upwash velocities near the ground. On the other hand, the  $0^\circ$  pumping blade generated relatively concentrated tip vortices with high induced velocities near the ground plane at the high thrust condition, but the tip vortices trailed at the lower thrust condition were significantly more diffused and induced relatively low upwash velocities; see Figs. 3.20 and 3.21. It is expected, therefore, that the wake of the  $0^\circ$  pumping blade would uplift significantly less sediment at the lower thrust condition than at the higher thrust condition. Furthermore, the results suggested that additional mass flow through the pumping slots would diffuse the stronger vortices produced at the higher thrust condition, ultimately yielding lower upwash velocities near the ground.

Another method of analysis is a wall velocity profile, such as the example shown in Fig. ???. In a wall velocity profile, a vertical cut is made through the flow field, and the velocities near the ground plane are plotted. When the cut intersects a tip vortex, the instantaneous profile shows high velocities (see cut A, Fig. ??). In contrast, a cut that does not intersect a vortex (e.g., cut B) shows relatively low velocities. In general, cut B



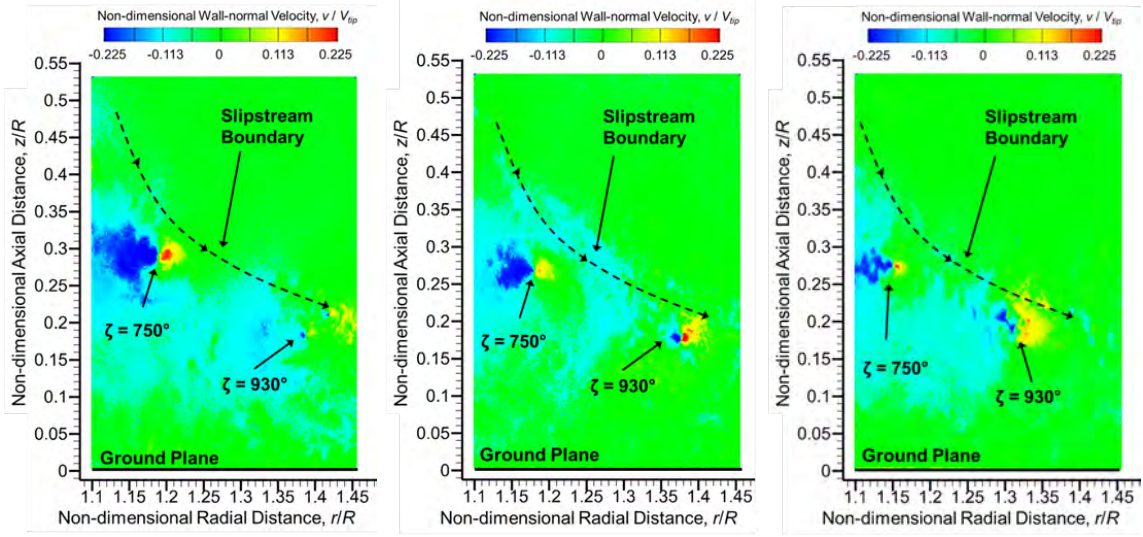
(a) Baseline non-pumping blade      (b)  $0^\circ$  exit slot orientation      (c)  $30^\circ$  exit slot orientation



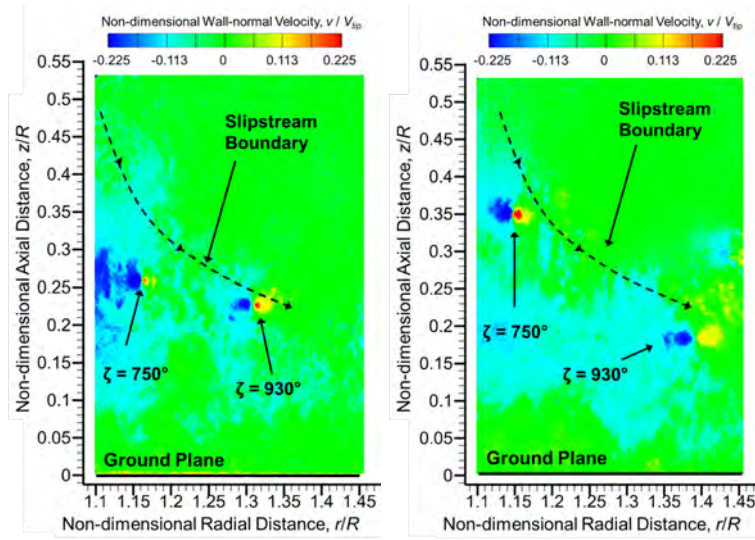
(d)  $45^\circ$  exit slot orientation      (e)  $60^\circ$  exit slot orientation

Fig. 3.16: Contours of instantaneous vorticity near the ground (ROI 2), with the reference blade at a blade azimuth angle ( $\psi_b$ ) of  $30^\circ$  and the rotor operating at a  $C_T/\sigma = 0.080$ , for the: (a) Baseline non-pumping blade; (b)  $0^\circ$  exit slot orientations; (c)  $30^\circ$  exit slot orientations; (d)  $45^\circ$  exit slot orientations; and (e) the  $60^\circ$  exit slot orientations.





(a) Baseline non-pumping blade (b)  $0^\circ$  exit slot orientation (c)  $30^\circ$  exit slot orientation



(d)  $45^\circ$  exit slot orientation (e)  $60^\circ$  exit slot orientation

Fig. 3.17: Contours of non-dimensionalized wall-normal velocity near the ground (ROI 2), with the reference blade at a blade azimuth angle ( $\psi_b$ ) of  $30^\circ$  and the rotor operating at a  $C_T/\sigma = 0.080$ , for the: (a) Baseline non-pumping blade; (b)  $0^\circ$  exit slot orientations; (c)  $30^\circ$  exit slot orientations; (d)  $45^\circ$  exit slot orientations; and (e) the  $60^\circ$  exit slot orientations.

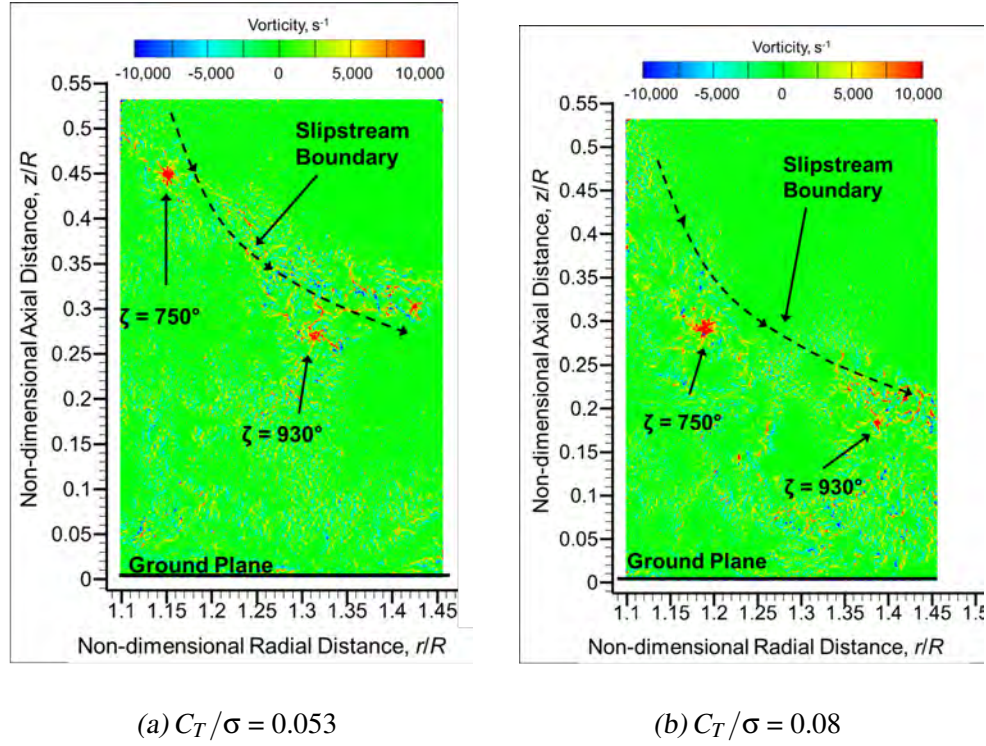


Fig. 3.18: Contours of instantaneous vorticity near the ground (ROI 2), for the rotor with the base-line blades at  $\psi_b = 30^\circ$  for each operating condition: (a)  $C_T/\sigma = 0.053$ ; (b)  $C_T/\sigma = 0.080$ .

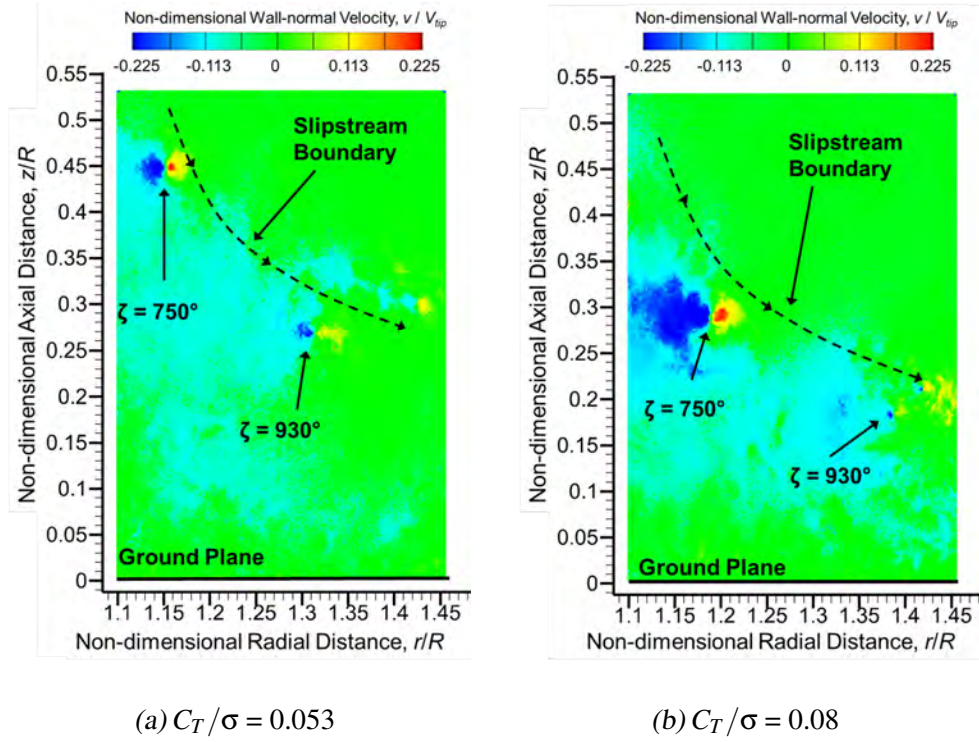


Fig. 3.19: Contours of non-dimensionalized wall-normal velocity near the ground (ROI 2), for the rotor with the baseline blades at  $\psi_b = 30^\circ$  for each operating condition: (a)  $C_T/\sigma = 0.053$ ; (b)  $C_T/\sigma = 0.080$ .

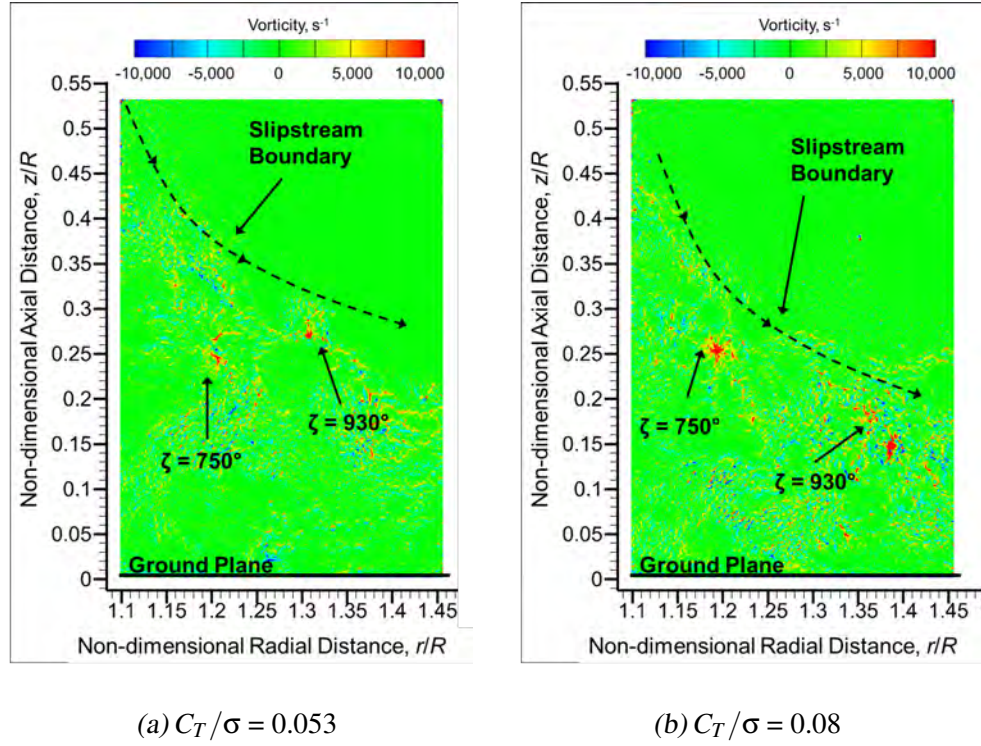


Fig. 3.20: Contours of instantaneous vorticity near the ground (ROI 2), for the rotor with the 0° pumping blades at  $\psi_b = 30^\circ$  for each operating condition: (a)  $C_T/\sigma = 0.053$ ; (b)  $C_T/\sigma = 0.080$ .



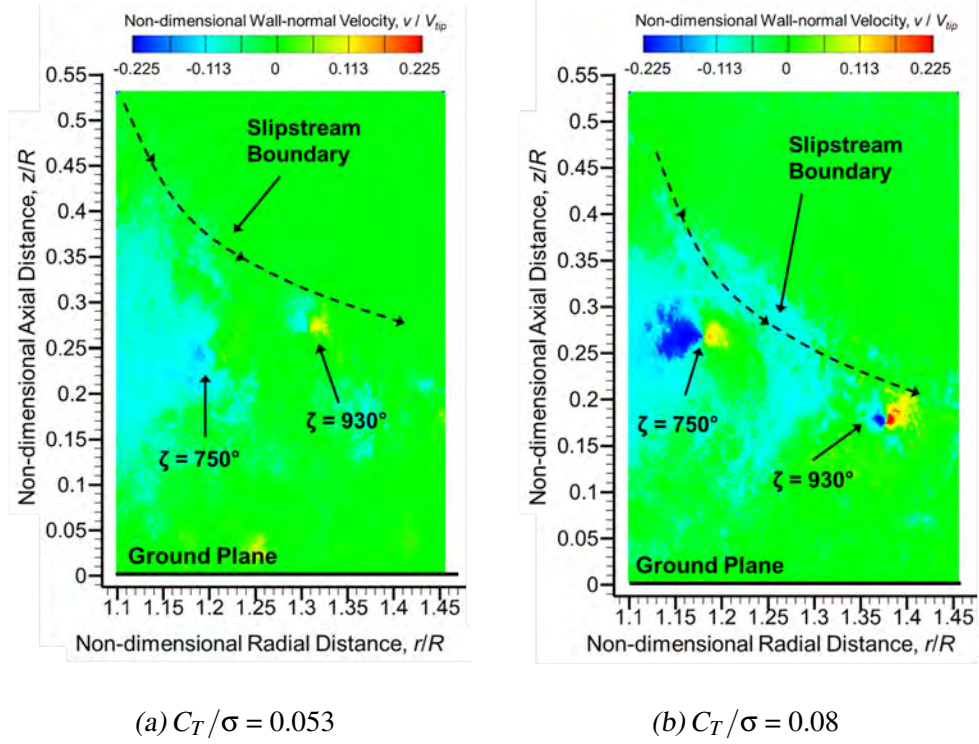


Fig. 3.21: Contours of non-dimensionalized wall-normal velocity near the ground (ROI 2), for the rotor with the  $0^\circ$  pumping blades at  $\psi_b = 30^\circ$  for each operating condition: (a)  $C_T/\sigma = 0.053$ ; (b)  $C_T/\sigma = 0.080$ .

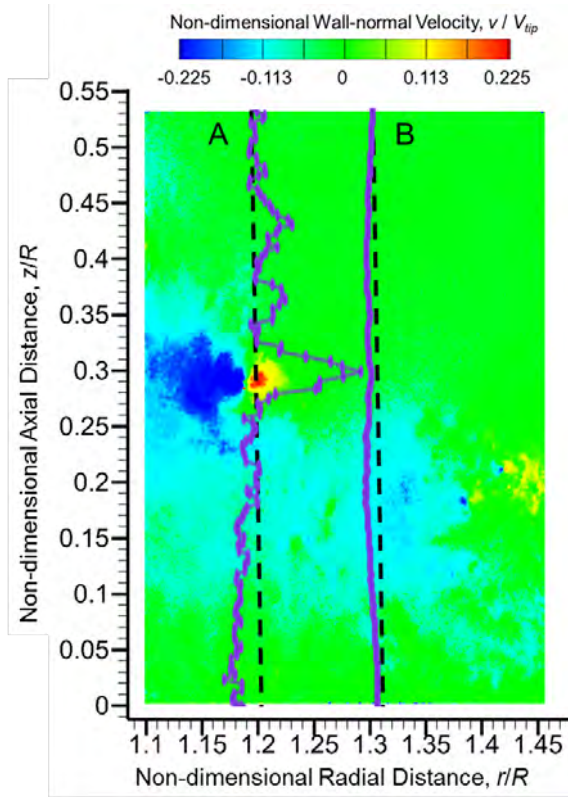


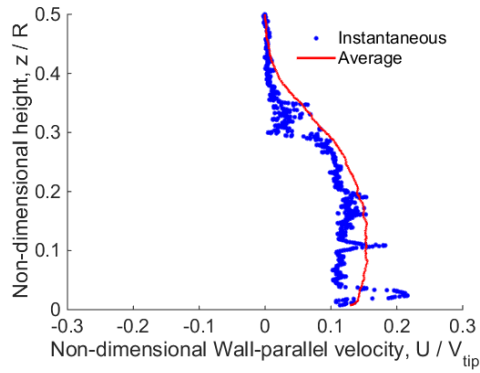
Fig. 3.22: Representative wall velocity profiles plotting wall-normal velocity in the flow field. Cut A intersects a tip vortex, while there is no tip vortex present in Cut B.

matches the average profile, while the high transient velocities present in cut A deviate significantly from the average profile. A flow field with relatively high transient velocities would be expected to uplift more sediment than a flow field in which the magnitude of difference between the transient and average flow velocities is lower.

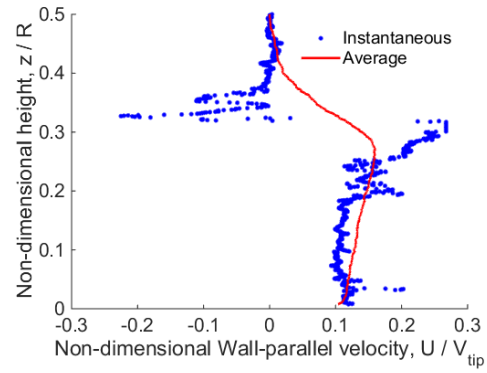
Figures 3.23 and 3.24 compare phase averaged and instantaneous velocities near the ground plane generated by the baseline blade and  $0^\circ$  pumping blade, respectively, at a blade loading coefficient of  $C_T/\sigma = 0.08$ . When the velocity profile did not cut through a tip vortex, the instantaneous profile nearly matched the average flow field. A wall-jet type flow was observed, but the induced velocities were relatively low (i.e., less than

$\pm 10\%$  tip speed). However, when the velocity profile cut through a tip vortex, high induced velocities were observed. The high wall-parallel velocities would be expected to contribute to creep and saltation, while the wall-normal velocities would be expected to cause significant sediment uplift.

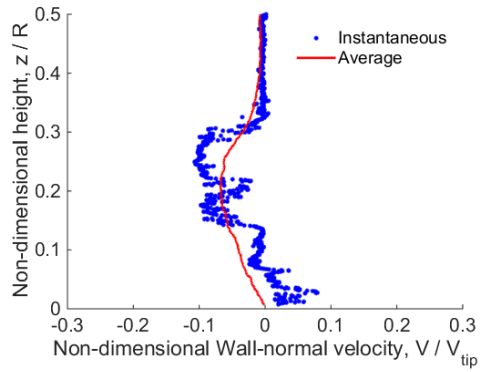
At the lower thrust condition, the baseline and  $0^\circ$  pumping blades generated similar average flow fields. The instantaneous velocity profiles closely matched the average profiles when the profiles did not cut through a tip vortex; see Figs. 3.25 and 3.26. However, the high instantaneous velocities associated with the tip vortices generated by baseline and pumping blades at low thrust differed significantly. While the tip vortex produced by the baseline blade still induced relatively high swirl velocities (e.g., it exhibited upwash velocities greater than 20% of the blade tip speed), the  $0^\circ$  pumping blade produced tip vortices with much lower swirl velocities. In particular, the upwash velocities induced by the pumping blade were only about half those produced by the baseline blade. It is expected that these lower upwash velocities would reduce the amount of sediment uplifted into the air.



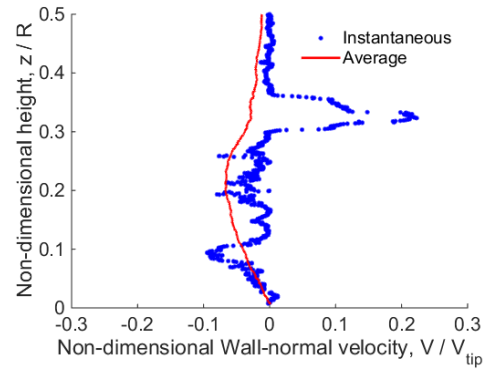
(a) Wall-parallel velocity, Cut B



(b) Wall-parallel velocity, Cut A

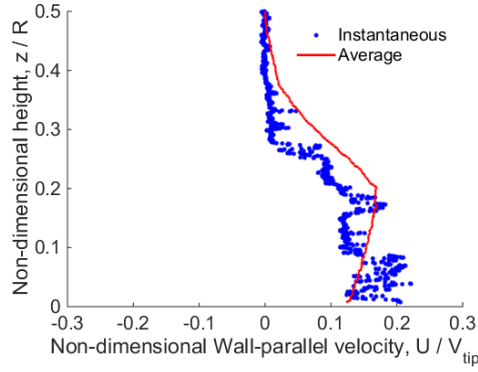


(c) Wall-normal velocity, Cut B

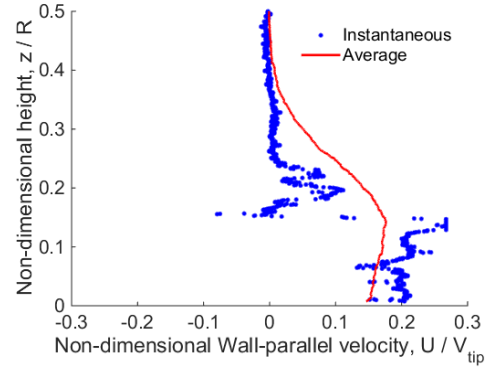


(d) Wall-normal velocity, Cut A

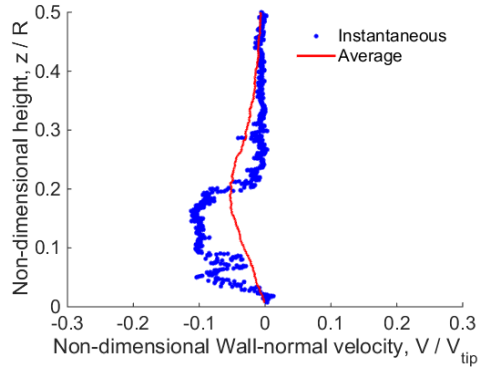
*Fig. 3.23:* Velocity profiles for the baseline, non-pumping blade at  $C_T/\sigma = 0.08$ : (a) Wall-parallel velocities with no tip vortex present, (b) Wall-parallel velocities with a tip vortex present, (c) Wall-normal velocities with no tip vortex present, and (d) Wall-normal velocities with a tip vortex present.



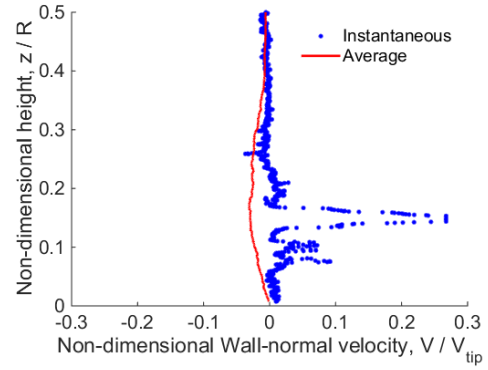
(a) Wall-parallel velocity, Cut B



(b) Wall-parallel velocity, Cut A

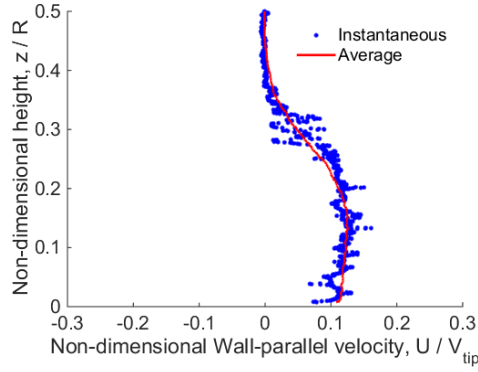


(c) Wall-normal velocity, Cut B

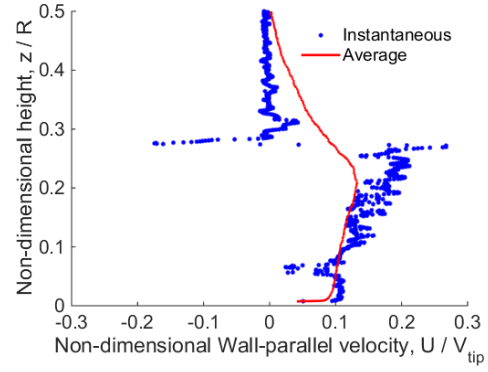


(d) Wall-normal velocity, Cut A

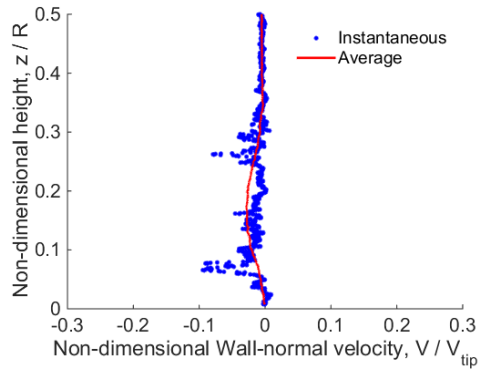
*Fig. 3.24:* Velocity profiles for the  $0^\circ$  pumping blade at  $C_T/\sigma = 0.08$ : (a) Wall-parallel velocities with no tip vortex present, (b) Wall-parallel velocities with a tip vortex present, (c) Wall-normal velocities with no tip vortex present, and (d) Wall-normal velocities with a tip vortex present.



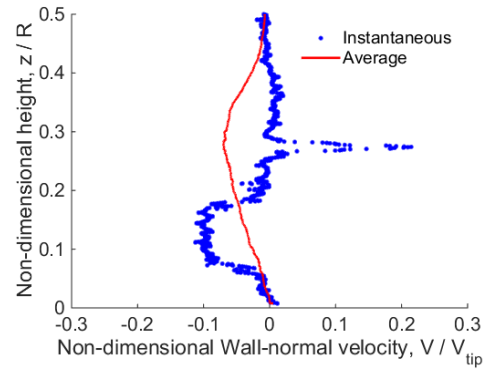
(a) Wall-parallel velocity, Cut B



(b) Wall-parallel velocity, Cut A

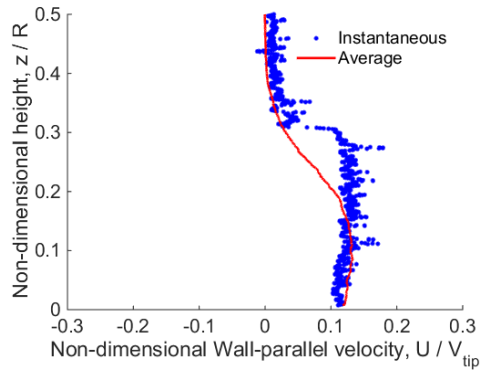


(c) Wall-normal velocity, Cut B

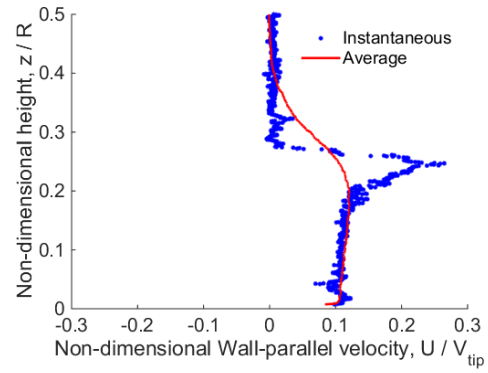


(d) Wall-normal velocity, Cut A

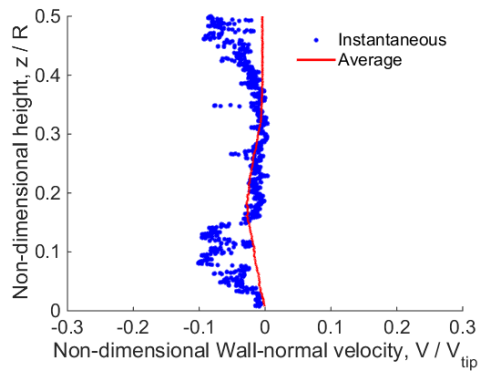
Fig. 3.25: Velocity profiles for the baseline, non-pumping blade at  $C_T/\sigma = 0.053$ : (a) Wall-parallel velocities with no tip vortex present, (b) Wall-parallel velocities with a tip vortex present, (c) Wall-normal velocities with no tip vortex present, and (d) Wall-normal velocities with a tip vortex present.



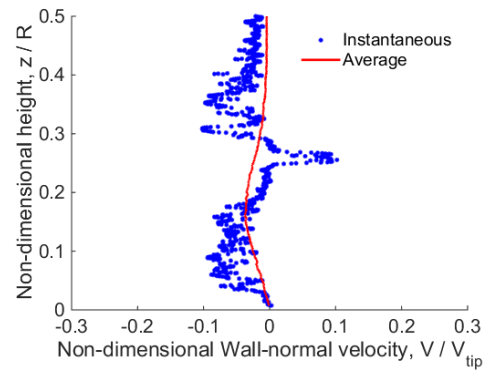
(a) Wall-parallel velocity, Cut B



(b) Wall-parallel velocity, Cut A



(c) Wall-normal velocity, Cut B



(d) Wall-normal velocity, Cut A

Fig. 3.26: Velocity profiles for the  $0^\circ$  pumping blade at  $C_T/\sigma = 0.053$ : (a) Wall-parallel velocities with no tip vortex present, (b) Wall-parallel velocities with a tip vortex present, (c) Wall-normal velocities with no tip vortex present, and (d) Wall-normal velocities with a tip vortex present.

## 4. CONCLUSIONS

High resolution phase-resolved flow visualization and particle image velocimetry experiments were conducted to understand the development and evolution of the blade tip vortices trailed from four different pumping blade designs. The effect of the tip vortices on the near-wall flow field was examined closely, as these vortices are directly responsible for sediment mobilization and uplift. Additionally, force and torque measurements were taken to calculate rotor thrust and power and to quantify changes in rotor performance caused by the changes in blade tip design. Detailed measurements near the rotor and near the ground plane were made in order to characterize the effect of centrifugal pumping and exit slot orientation on the flow field. The following conclusions were drawn:

1. Similarly to the slotted tip blade [5,6], the pumping blade designs incurred a slight performance penalty caused by profile losses associated with the exit slots. However, at higher thrust conditions, the pumping blade designs showed similar power requirements to that of the baseline blade, suggesting that they experienced a lower induced power penalty. The  $30^\circ$ ,  $45^\circ$ , and  $60^\circ$  slotted pumping blade designs were found to have slightly degraded performance when compared to the  $0^\circ$  pumping blade, as the positive exit slot orientation created a negative thrust effect due to mass flow through the pumping slots. When this negative thrust effect was mathe-



matically removed, all pumping blade designs were found to exhibit similar performance characteristics.

2. When the rotors were operated at a higher blade loading coefficient (i.e.,  $C_T/\sigma = 0.08$ ), the pumping blade designs initially ( $\zeta \leq 30^\circ$ ) produced tip vortices more diffused than those generated by the baseline blade. The  $0^\circ$  and  $30^\circ$  in particular were the most successful at initially diffusing the tip vortices. However, at the higher thrust condition, the pumping blades did not fully diffuse the tip vortices, but instead prolonged their initial formation. Ultimately, the tip vortices reintensified in ground effect, where they induced relatively high upwash velocities which would be expected to significantly contribute to sediment uplift in a brownout environment.
3. Because the pumping blades did not effectively diffuse the tip vortices at the higher thrust condition, the effect of mass flow rate through the pumping slots was examined. To simulate a higher mass flow rate through the slots, the baseline and  $0^\circ$  pumping blade were tested at a lower blade loading coefficient of  $C_T/\sigma = 0.053$ , as this operating condition lowered tip vortex strength while maintaining mass flow rate. It was found that the baseline blade generated similar flow fields at both thrust conditions, with tip vortices that rolled up relatively quickly (i.e.,  $\zeta \leq 30^\circ$ ) and persisted to the ground. On the other hand, the tip vortices trailed by the  $0^\circ$  pumping blade were significantly more diffused at the lower thrust condition than at the higher thrust condition. Specifically, the pumping blades generated diffused tip vortices with significantly lower induced swirl velocities at the lower blade loading coefficient. These differences persisted to the ground plane, where at the lower

thrust condition, the  $0^\circ$  pumping blade induced lower upwash velocities, suggesting that the pumping blade would mitigate sediment uplift.

#### *4.1 Recommendations for Future Work*

1. This work has shown that the pumping blades with exit slots oriented above the horizontal did not significantly diffuse the tip vortices at the higher thrust condition. Additionally, the mass flow through the upward exit slots adversely affected rotor performance. Further research could investigate similarly designed blades with downward oriented blades, with the goal of investigating whether a downward exit slot orientation might better diffuse tip vortices or positively affect rotor performance.
2. The results showed that mass flow through the pumping slots significantly affected vortex diffusion. New experiments could be carried out with wider pumping slots, thereby increasing the mass flow. This experiment could be used to better understand the effect of mass flow through the pumping slots on vortex diffusion.
3. This experiment was carried out on a small scale. Larger scale experiments of a similar nature would establish whether the results observed hold true for larger rotors and Reynolds numbers closer to those actually used in rotorcraft operations.
4. A close examination of the flow exiting the tip slots would enhance the current understanding of the fluid dynamics associated with the pumping slots. This could be achieved using PIV measurements in the rotor plane, focused on the rotor tips.

5. Finally, the current work was carried out in a single-phase environment, and the effects of the blade design on sediment uplift were inferred, based on previous work. Dual-phase experiments, which would test the rotor in an environment with a sediment bed, would be required to directly assess the effectiveness of different blade designs on diffusing the tip vortex.

## REFERENCES

- [1] Lee, T. E., Leishman, J. G., and Ramasamy, M., “Fluid Dynamics of Interacting Blade Tip Vortices With a Ground Plane,” American Helicopter Society 64th Annual Forum Proceedings, April 20–May 1, 2008.
- [2] Milluzzo, J. I., “Contributions Towards the Detailed Understanding of Rotor Flow Fields in Ground Effect Operation,” Technical report, Ph.D. dissertation, Department of Aerospace Engineering, University of Maryland at College Park, USA, 2014.
- [3] Sydney, A., and Leishman, J. G., “Time-Resolved Measurements of Rotor-Induced Particle Flows Produced by a Hovering Rotor,” *Journal of the American Helicopter Society*, Vol. 59, (2), 2014, pp. 1–16.
- [4] Milluzzo, J., Sydney, A., Rauleder, J., and Leishman, J. G., “In-Ground-Effect Aerodynamics of Rotors with Different Blade Tips,” 66th Annual Forum Proceedings of the American Helicopter Society, May 10–13, 2010.
- [5] Han, O. Y., and Leishman, J. G., “Performance Measurements of a Rotor Blade With a Slotted Tip,” American Helicopter Society 60th Annual Forum Proceedings, June 2004.

- [6] Han, O. Y., and Leishman, J. G., “Experimental Investigation of Tip Vortex Alleviation Using a Slotted Tip Rotor Blade,” *AIAA Journal*, Vol. 42, (4), 2004, pp. 523–535.
- [7] Tritschler, J., Syal, M., Celi, R., and Leishman, J. G., “A Methodology for Rotor Design Optimization for Rotorcraft Brownout Mitigation,” 66th Annual Forum Proceedings of the American Helicopter Society, May 10–13, 2010.
- [8] Tritschler, J., Syal, M., Celi, R., and Leishman, J. G., “The Effect of Number of Blades on Optimum Rotor Design for Brownout Mitigation,” Future Vertical Lift Aircraft Design Conference, January 18–20, 2012.
- [9] Mapes, P., Kent, R., and Wood, R., “DoD Helicopter Mishaps FY85-05: Findings and Recommendations,” Technical report, U.S. Air Force, Washington, DC, April, 2008.
- [10] Technical report, National Transportation Safety Board, NTSB Accident Briefs: LAX01LA283, LAX01LA304, LAX04LA285, SEA05CA173”, year =.
- [11] Ramasamy, M., and Leishman, J. G., “Interdependence of Diffusion and Straining of Helicopter Blade Tip Vortices,” *Journal of Aircraft*, Vol. 41, (5), September 2004, pp. 1014–1024.
- [12] Johnson, B., Leishman, J. G., and Sydney, A., “Investigation of Sediment Entrainment Using Dual-Phase, High-Speed Particle Image Velocimetry,” *Journal of the American Helicopter Society*, Vol. 55, (4), 2010, pp. 1–16.

- [13] Harrison, R., Stacey, S., and Hansford, B., “BERP IV: The Design, Development and Testing of an Advanced Rotor Blade,” American Helicopter Society 64th Annual Forum Proceedings, April 29–May 1, 2008.
- [14] Leishman, J. G., and Han, O. Y., “Rotor Blade System With Reduced Blade-Vortex Interaction Noise,” Technical Report 6,948,906 B2, U.S. Patent, September 27, 2005.
- [15] Watkins, C. B., and Dutta, S. K., “Numerical and Experimental Simulation of Circulation Control Rotor Pneumodynamics,” AIAA Aircraft Design, System and Technology Meeting, Fort Worth, TX, October 17–19, 1983.
- [16] Watkins, C. B., Reader, K. R., and Dutta, S. K., “Pneumodynamic Characteristics of a Circulation Control Rotor Model,” 2nd Decennial Specialist’ Meeting on Rotorcraft Dynamics, NASA Ames Research Center, Moffett Field, CA, November, 1984.
- [17] Lorber, P. F., and Lord, W. K., “Centrifugal Air Flow Control,” Technical Report 6,203,269 B1, U.S. Patent, March 20, 2001.
- [18] Leishman, J. G., *Principles of Helicopter Aerodynamics*, Cambridge University Press, New York, NY, 2006.
- [19] Landgrebe, A. J., “An Analytical Method for Predicting Rotor Wake Geometry,” Presented at the AIAA/AHS VTOL Research, Design & Operations Meeting, February 1969.

- [20] Landgrebe, A. J., “An Analytical Method for Predicting Rotor Wake Geometry,” *Journal of the American Helicopter Society*, Vol. 14, (4), 1969, pp. 20–32.
- [21] Landgrebe, A. J., “An Analytical and Experimental Investigation of Helicopter Rotor Performance and Wake Geometry Characteristics,” Technical Report 24, US-AAMRDL TR, 1971.
- [22] Landgrebe, A. J., “The Wake Geometry of a Hovering Rotor and Its Influence on Rotor Performance,” *Journal of the American Helicopter Society*, Vol. 17, (4), 1972, pp. 2–15.
- [23] Milluzzo, J., and Leishman, J. G., “Development of the Turbulent Vortex Sheet in the Wake of a Hovering Rotor,” 69th Annual Forum Proceedings of the American Helicopter Society, May 21–23, 2013.